Experimental and model angular distributions of one- and two-electron capture processes in 0.5–20 eV/u Ar^{4+}-Ar collisions

C. Biedermann
Department of Physics, University of Tennessee, Knoxville, Tennessee 37996-1200 and Oak Ridge National Laboratory, Oak Ridge, Tennessee 37831-6377

H. Cederquist and L. R. Andersson
Manne Siegbahn Institute of Physics, S-10405 Stockholm, Sweden

J. C. Levin, R. T. Short, S. B. Elston, and J. P. Gibbons
Department of Physics, University of Tennessee, Knoxville, Tennessee 37996-1200 and Oak Ridge National Laboratory, Oak Ridge, Tennessee 37831-6377

H. Andersson and L. Liljeby
Manne Siegbahn Institute of Physics, S-10405 Stockholm, Sweden

I. A. Sellin
Department of Physics, University of Tennessee, Knoxville, Tennessee 37996-1200 and Oak Ridge National Laboratory, Oak Ridge, Tennessee 37831-6377
(Received 5 January 1990)

We have measured and calculated state-resolved angular distributions of one- and two-electron-capture processes in 0.5–20 eV/u Ar^{4+}-Ar collisions. The experimental energy-gain spectra show single-electron capture to six unresolved $4p$ LS terms, while no trace of a $4s$ population was found for laboratory collision energies below 200 eV. Semiclassical trajectory calculations, using a seven-channel Landau-Zener model for the probability flux on the multivalued deflection functions, show that the oscillations in the experimental $4p$ angular differential cross section are due to multiple rainbow scattering and that interference effects play a limited role. Experimental and calculated $4p$ angular distributions compare nicely over the whole energy range. For energies above 150 eV, true double-capture and transfer ionization with angular distributions consistent with a two-step electron-transfer process appear within the $\pm 9°$ experimental acceptance.

I. INTRODUCTION

One of the main goals of the recent activity in the field of slow collisions between highly charged ions and neutral atoms is to identify dominant charge-transfer mechanisms. Several experimental methods are used for this purpose. Measurements of total charge-exchange cross sections usually provide only information through model comparisons,[1] while post-collisional energy-gain measurements directly reveal the distribution of final projectile capture states.[2] The more intensity demanding methods of electron-emission[3] and photon-emission[4] spectroscopy yield the same distributions, more indirectly but with higher resolution. Experimental state-selective projectile angular distributions are the most powerful means to study the finer details of electron-transfer mechanisms.[5,6] In particular, it may be possible to decide when a full quantum-mechanical calculation is necessary[7] and when a semiclassical one is sufficient. The sensitivity of angular differential cross sections to the shapes of active potential curves, and the probabilities for transitions between them, increase with decreasing velocity. Therefore experiments at low and very-low collision energies are called for. Recently, a new technique for studies of state-resolved angular distributions in very-slow collisions was introduced,[8,9] and the first data on single-electron capture in Ar^{4+}-Ar collisions at laboratory energies down to 19 eV (0.48 eV/u) were presented.[9,10] In order to fulfill the claim that the experimental results may give decisive guidance for theoretical efforts, we present multichannel Landau-Zener calculations for the same angular distributions. We further extend the measurements and the calculations to two-electron processes, with the ambition of determining the relative importance of one- and two-step electron transfer.

Very slow collisions between highly charged ions and atoms have been studied by means of ion trap[11] or merged-beam[12] techniques. By both methods it is, however, difficult to extract information on the kinematics of the collision, and these kinds of experiments are limited to the study of total charge-exchange cross sections. In the present experiment, we use a beam of very low laboratory energy for simultaneous measurements of the post-collisional projectile energy and angle. With the additional knowledge of the incident-beam energy, the heavy-particle kinematics may be determined unambigu-

ously and projectile capture-state-resolved angular distributions can be inferred. Earlier investigations on state-selective angular distributions have mostly been performed at substantially higher energies[13,14] or on collision systems for which the capture states are known from complementary energy-gain experiments.[15,16] The Ar^{4+}-Ar system has been studied by means of the energy-gain technique by Giese *et al.*,[17] Puerta *et al.*,[18] Koslowski and Huber,[19] and Hvelplund and Cederquist[20] at energies of 2180, 800, 800, and down to 160 eV, respectively.

In a very slow collision, the inelasticity Q of the charge-transfer process is of the same order of magnitude as the incident center-of-mass kinetic energy. Electronic and nuclear motion can be separated due to the velocity difference and the quasimolecular framework is appropriate for describing electron transfer both in slow and very slow collisions. A close interplay between experiment and theory has led to the development of several successful models for absolute charge-exchange cross sections and distributions on final capture states. The basic idea of electron transfer at the internuclear distance where the Stark-shifted binding energy of the least bound target electron reaches the top of the internuclear potential barrier has been applied to consecutive one-electron transfers in the static extended classical over-barrier model.[21,22] In this model, estimates of ranges for inelasticities and projectile scattering angles for one-, two-, and multiple-electron transfer processes can be deduced by assuming quasicontinua of capture states.[23,24] The dynamic Landau-Zener model[25] gives velocity and impact-parameter-dependent transition probabilities at avoided crossings of adiabatic potential curves, provided that the magnitudes of the energy splittings are known. In this model, electron transfer is strongly localized to regions of avoided crossings and the motion of the nuclei follow classical trajectories, governed by the interatomic potential-energy diagram. Thus the Landau-Zener model is well suited for comparative calculations of state-specific angular distributions if the atomic (ionic) energy-level diagrams are known and if few quasimolecular potentials are active. Olson and Salop[26] derived a semiempirical formula for the single-capture quasimolecular adiabatic energy splitting from *ab initio* calculations of matrix elements for bare-nuclei atomic-hydrogen systems. Taulbjerg[27] modified this expression for the case of partially stripped projectiles. A further modification, which takes the angular momentum and spin-selection rules of open-shell projectiles and targets into account, is presented in this paper.

The present semiclassical multichannel Landau-Zener calculations assume seven open single-capture channels and one double-capture channel assigned to the experimentally determined average Q value for two-electron processes. The model angular differential cross sections compare very nicely with the experimental ones. This comparison shows that the prominent structures in the experimental angular distributions are due to multiple rainbow scattering and not due to Stueckelberg oscillations. The interatomic potentials of the outgoing channels are of the Coulomb type. In the incident channel and the exiting single-capture channels, a polarization energy term is added. A universal one-parameter polarization damping function reduces the attraction of the incident and single-capture potentials at small internuclear distances (R). The parameter λ is set to a unique value by requiring that the forward peaks of the calculated single-capture angular distributions agree with the measured ones over the entire 19–800-eV laboratory energy range.

The dominant two-electron processes are, in general, true double capture and transfer ionization. In the former, two electrons are transferred between the target and a nonautoionizing projectile state, while the latter process involves emission of one electron. From the measured Doppler shifts of unperturbed atomic emission lines, it is clear that transfer ionization, in slow collisions, proceeds as capture to a doubly excited projectile state that autoionizes at large internuclear separation.[28] The relative importance of one and two-step processes for population of such intermediate states is currently under discussion.[29–31] In the one-step process, electron capture is depicted as taking place at a single well-localized avoided crossing of adiabatic potential curves. This kind of transition may, in principle, be due to the correlation (repulsion) between the two captured electrons.[29] In the two-step process the transfer is described as two consecutive one-electron transitions taking place at avoided crossings that are well separated. With the aid of post-collisional projectile angular distributions, it is possible to distinguish between the two mechanisms since the latter usually leads to larger deflection angles. A large number of experiments have shown domination of the two-step process for collision systems with a high density of final capture states.[13,14] Here, we demonstrate the importance of two-step capture in 150–800-eV Ar^{4+}-Ar true double-capture and transfer-ionization processes.

In Sec. II we give a detailed account of the part of the experimental technique that concerns post-collisional energy and angular analysis, including the performance of a new 64° cylindrical energy analyzer of ~40 mm radius. The production of the well-collimated, very-slow beam with a narrow energy distribution has been described before[8] and will only be discussed briefly. The theoretical model is presented in Sec. III with emphasis on the influence of atomic angular momentum and spin on the off-diagonal diabatic matrix elements. Section IV is devoted to comparisons between experimental and calculated state-selective angular distributions. In Sec. IV A we show that the experimental angular distributions for single-electron capture to the $4p$ Ar^{3+} state in the energy range 19–200 eV can be explained in terms of dual rainbow scattering. Incoherent addition of the calculated angular differential cross sections of the six open $4p$ LS terms is shown explicitly for one collision energy. Moreover, the influence on the calculated angular distribution by various modifications of the interatomic potential curves is investigated and we show that the influence of Stueckelberg oscillations is small at the present experimental resolution. The inclusion of double-capture potential curves (inferred from our energy-gain spectra) has a very limited effect on the calculated single-capture an-

gular distributions, which then may be treated separately within our range of angular acceptance. On the other hand, the two-electron angular distributions of Sec. IV B are closely connected to those of single-electron capture and we conclude that two-step electron-transfer mechanisms dominate in the collision-energy regime 150–800 eV. Finally, in Sec. IV C we show that the angular and energy-gain distributions for true double capture and transfer ionization agree, indicating that the same population mechanism for similar doubly excited intermediate states is active in both processes.

II. EXPERIMENTAL TECHNIQUE

The experimental setup consists of a differentially pumped recoil-ion source, a Wien filter, an effusive gas jet, and an energy analyzer, followed by a two-dimensional position-sensitive detector for registrations of collision inelasticities and angular distributions (Fig. 1). A pump beam of 30-MeV Cl^{5+} ions from the Oak Ridge National Laboratory EN-12 tandem Van de Graaff accelerator was post stripped and directed into a differentially pumped gas cell in order to produce recoil ions.[8] Alternatively, we produced recoil ions with 2-keV electrons from a Perkin-Elmer PHI-04-015 electron gun. The Ar recoil ions are extracted from the production gas cell by means of an electric field. In order to achieve good resolution in the post-collisional energy-gain spectra, the very-slow ion beam must have a narrow energy distribution. This is achieved by means of a low extraction field and a well-collimated pump beam in the recoil-ion production region. The gas cell is followed by a six-element linear-acceleration region and a Wien filter, where the first elements of the former are located inside a differential pump step. By means of the perpendicular electric and magnetic fields of the filter, the velocities of the passing ions are analyzed. Since the ions were first accelerated by a constant electric field, we separate the charge-to-mass ratios of the recoil ions at the exit aperture of the filter. The separated beam is retarded to ground potential by means of a ten-element linear-retardation lens before it enters the collimator. At the target the very-slow ion beam has a maximum diameter of ~ 1 mm and a maximum angular divergence of $\pm 0.5°$. The collision energy of the beam is determined by the potential difference between the region where the recoil ions are created, V_{beam}, and the gas-jet target, held at ground potential. The initial energies of recoil ions produced in the present fast heavy-ion collisions have been measured[32] to be below 0.5 eV. The contribution to the energy spread from the finite 0.4 mm width of the pump beam in the extraction field (< 3 V/cm) amounts to $0.12q$ eV, where q is the charge state of the projectile. A more detailed description of the ion source and its performance is given in Ref. 8. For the production of recoil ions by electron impact, we find a maximum for production of Ar^{4+} at impact energies around 2 keV, in agreement with the results of Hippler *et al.*[33] The cross section for producing Ar^{4+} by heavy-ion impact[34] is higher than with electron impact, but the electron current is higher than that achieved with the fast heavy-ion beam with the result that Ar^{4+} production rates are similar. We measure Ar^{4+} particle currents of $\sim 10^3$ and $\sim 10^4$ s^{-1} at beam energies of 19 and 800 eV, respectively.

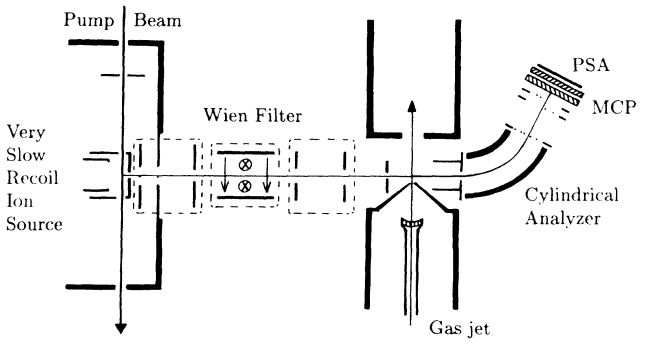

FIG. 1. A schematic of the experimental setup. Argon recoil ions are produced in the gas cell by either a beam of 30-MeV Cl^{5+} ions or by 2-keV electrons. After extraction by means of a weak electric field, the ions are accelerated to the negative potential of the charge-state-separating Wien filter. The potential at the fast ionizing beam determines the collision energy, since the Ar^{4+} beam is retarded to ground potential before it crosses the collimated gas-jet target. The post-collisional energy and charge-state distributions of the very-slow beam are analyzed by means of a 40.5-mm-radius cylindrical energy analyzer and a two-dimensional position-sensitive detector. After the final drift region, which is terminated by a grid at the analyzer's focal plane, the ions are accelerated to an energy of about $2q$ keV before they hit the multichannel-plate detector (MCP). The last channel plate is followed by a two-dimensional position-sensitive anode (PSA).

The very-slow ion beam crosses the effusive gas jet at right angles. The differentially pumped gas-jet target is furnished through a concave glass-capillary array, which is focused at the crossing with the very-slow ion beam. In order to resolve structures in the post-collisional angular distributions, the thermal velocity spread of the gas jet has to be diminished in the direction of angular dispersion. This is achieved by collimating the gas jet, which has a diameter of about 1 mm at the intersection point and a divergence of less than 10°. With the present setup, it is possible to keep the pressure in the main chamber at 5×10^{-7} Torr with a target pressure of ~ 2 mTorr and a pressure of ~ 6 mTorr in the production gas cell.

After the interaction of the very-slow ion beam with the gas-jet target, the charge states, energies, and scattering angles of the emerging projectiles were analyzed by either a 30° parallel-plate electrostatic analyzer[9] or a cylindrical energy analyzer (Fig. 1), followed by a two-dimensional position-sensitive detector (PSD). Both analyzers are focusing only in the plane of energy dispersion. This makes it possible to obtain the energy-gain information from the position along the axis of energy dispersion in the focal plane, while the position in the perpendicular direction is related to the scattering angle. The energy and angular distributions in the focal plane are mapped onto the two-dimensional position-sensitive detector by a short acceleration region, giving the ions an

energy of $2q$ keV in order to increase the detection efficiency. The position-sensitive detector consists of a two-stage microchannel-plate (MCP) array followed by a resistive anode. The projectile position is decoded from the accumulated charge recorded at the four corners of the anode. Due to the many meshes that the ion beam has to pass at small angles, the transmission of the 30° parallel-plate electrostatic analyzer is quite low. For this reason it was replaced by a 64° cylindrical analyzer with a radius of $R_1 = 36.5$ mm for the inner sector and $R_2 = 44.5$ mm for the outer one. The analyzer is preceded by a drift region of 36 mm (the separation between the target region and the field plates of the analyzer), and a vertical slit of 1.7 mm width just upstream of the analyzer plates limits the acceptance in the plane of energy dispersion to $\pm 1.4°$. A drift region of 22 mm length after the sector plates is terminating at the focal plane of the analyzer. The design value for the relative energy resolution of the cylindrical analyzer is 1.3%, while the measured peak width corresponds to a resolution of 1.6%, for ions traveling along the central trajectory of the analyzer. For the parallel-plate analyzer the corresponding values are 3% and $\simeq 4\%$, respectively. The calculated and measured values for the angular resolution are both about $\pm 0.5°$. The angular acceptance of the present setup is limited to about $\pm 9°$ by the diameters of the microchannel plates. Apart from a higher transmission and a better energy resolution for the cylindrical analyzer, no differences between the energy or angular distributions obtained with the two analyzers were observed.

In Fig. 2 an image on the PSD for single-electron capture in 40-eV Ar^{4+}-Ar collisions is shown. The horizontal position of the image can be related to the energy gain ΔE of the projectile, while the vertical position is a function of the scattering angle, θ. Only Ar^{3+} ions are seen in the image since the primary Ar^{4+} ions are deflected outside the detector range for this particular setting of the analyzer voltage V_a. Through integration of the two-dimensional angular energy distribution, the energy-gain spectrum for a particular range of angles, or the angular distribution within a range of energy-gain values, is obtained. The energy E of a beam of charge q following the central path through the analyzer is given by

$$E = q\frac{V_a}{K} , \tag{1}$$

where K is the analyzer constant for the central trajectory

$$K = 2\ln\frac{R_e}{R_1} \simeq 0.396 . \tag{2}$$

The energy calibration is obtained by recording the position x on the detector for the incident Ar^{4+} beam and the corresponding analyzer voltage V_a for a fixed energy qV_{beam}, thus giving a calibration function $f(x) = V_{\text{beam}}/V_a$. The calibration function is, simply, the inverse of K as a function of the horizontal beam position x on the detector. The energy gain ΔE of a projectile, which changes its charge from q to q', is then given by

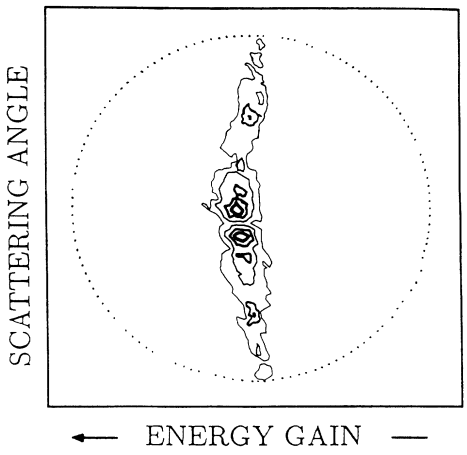

FIG. 2. The image on the detector following single-electron capture in 40-eV Ar^{4+}-Ar collisions. The horizontal beam position can be related to the post-collisional projectile energy gain ΔE, while the vertical position is a function of the scattering angle θ. Only Ar^{3+} ions contribute to the image, since the primary Ar^{4+} beam falls outside the range of the detector at this particular setting of the analyzer voltage. The contour lines are plotted at 20, 40, 60, and 80% of the maximum intensity. The edge of the channel plate is indicated by a circle.

$$\Delta E(x) = q' f(x) V_a' - q f(x_0) V_a , \tag{3}$$

where x_0 is the position of the primary beam (with charge q) at the analyzer voltage V_a, and V_a' is the analyzer voltage when recording the charge-exchanged beam (q') at the position x. The angular calibration is obtained from the (vertical) position of the beam along the direction perpendicular to the energy dispersion and the calculated trajectory length from the gas jet to the detector. The inelasticity Q of a collision is equal to the difference between the kinetic energies of the projectile and the target before and after the collision. The shift of the peak to smaller energy-gain values at large scattering angles in Fig. 2 may be calculated by means of classical two-body kinematics.[35] When the projectile and the target are of equal masses, or when the target is heavier than the projectile, this shift in energy gain is small but detectable for angles that can be recorded in this experiment.

III. THEORETICAL MODEL

We model the Ar^{4+}-Ar collision system by means of an extended version of the multistate semiclassical collision model described by Andersson *et al.*[36] While the original model neglects all elastic interactions in the initial channel and retains only Coulomb repulsion in the final channels, the polarization interaction cannot be neglected in the present energy range. In addition, screened Coulomb terms accounting for the penetration of the ionic cores at small internuclear distances are introduced as an option. The diabatic potentials for the initial and the final single-electron-capture channels (in atomic units) are

$$V_0(R)=-\frac{\alpha_I q^2}{2R^4}[1-\exp(-\lambda R)]^4+\frac{Z_{\text{core}}q}{R}\exp(-\kappa_I R) \tag{4}$$

and

$$V_k(R)=\frac{(q-1)}{R}-\frac{\alpha_F(q-1)^2}{2R^4}[1-\exp(-\lambda R)]^4 + \frac{Z_{\text{core}}(q-1)}{R}\exp(-\kappa_F R)-Q_k\ , \tag{5}$$

respectively. The projectile charge is denoted by q, α_I and α_F are the polarizabilities of ground-state Ar and Ar^+, respectively, and Q_k is the energy defect of the final channel k. The polarizabilities[37] used here are $\alpha_I=11.1a_0^3$ and $\alpha_F=5.4a_0^3$. The factor multiplying the polarization terms in Eqs. (4) and (5) is introduced in order to suppress the domination of R^{-4} terms at small internuclear distances. λ^{-1} thus sets the typical distance for this damping term to become effective. In principle, λ could be different for each channel but, in order to keep the number of free parameters low, we use the same value for all channels. We assume that the projectile ion penetrates the outer shell of the target at a distance characterized by the ionization potentials I_{Ar} and I_{Ar^+} of Ar and Ar^+, respectively. $Z_{\text{core}}=6$ is therefore the charge of the target core (p shell and $\kappa_I=(2I_{\text{Ar}})^{1/2}=1.07$ and $\kappa_F=(2I_{\text{Ar}^+})^{1/2}=1.42$. The core-penetration potentials were included in order to investigate their influence on single-electron-capture angular distributions. Since this influence was found to be rather limited (cf. Sec. IV), penetration effects were ignored in the main calculations for single- and double-electron capture. The innermost final channel V_k (i.e., the one with largest Q_k) is assumed to couple fully adiabatic to the initial channel V_0, ensuring reversal of the radial motion and overall probability conservation. The potential curves constructed from Eqs. (4) and (5) without the penetration terms are shown in Fig. 3. In the figure, one double-capture channel is also present. This channel is discussed further below.

The important mechanism driving the charge-transfer reaction is assumed to be the relative radial motion of the nuclei. The importance of the rotational coupling usually decreases with lower velocity at large internuclear distance and therefore it is neglected for the present very-low collision velocities. We further assume that the transitions are localized to the curve crossings of the diabatic states of the electronic Hamiltonian and that the curve crossings are well isolated from each other. The multichannel system can then be treated as a series of effective two-state systems. The Landau-Zener expression for the diabatic transition probability when making a single passage at a curve crossing is[25]

$$p=\exp\left[\frac{-2\pi H_{12}^2}{v|\Delta F|}\right]\ . \tag{6}$$

Here H_{12} is the matrix element of the electronic Hamiltonian H_{el} taken between the two diabatic states, v is the relative radial velocity, and ΔF the difference in slopes of the two diabatic potential curves. All quantities are evaluated at the crossing radius.

The multichannel Landau-Zener (MCLZ) formalism gives the probabilities $P_k^{(j)}$ for a collision exiting in final channel k via the classical path (j) of the several possible paths (for details see Ref. 36). The scattering amplitude for a collision exiting in the final channel k is written

$$F_{0k}=\sum_j f_{0k}^{(j)}=\sum_j\left[P_k^{(j)}\frac{d\sigma_{0k}^{(j)}}{d\Omega}\right]^{1/2}\exp(iA_k^{(j)})\ . \tag{7}$$

In Eq. (7), $d\sigma_{0k}^{(j)}/d\Omega$ is the classical differential cross section for scattering along path j, and $A_k^{(j)}$ is the classical action for this path. In the original applications of this model the differential cross section for exiting in channel k was obtained by squaring Eq. (7) and neglecting the (by assumption) rapidly oscillating interference terms. Here we keep the interference terms to check if the experimentally observed oscillatory structure can be understood in terms of interference oscillations. The differential cross section is thus

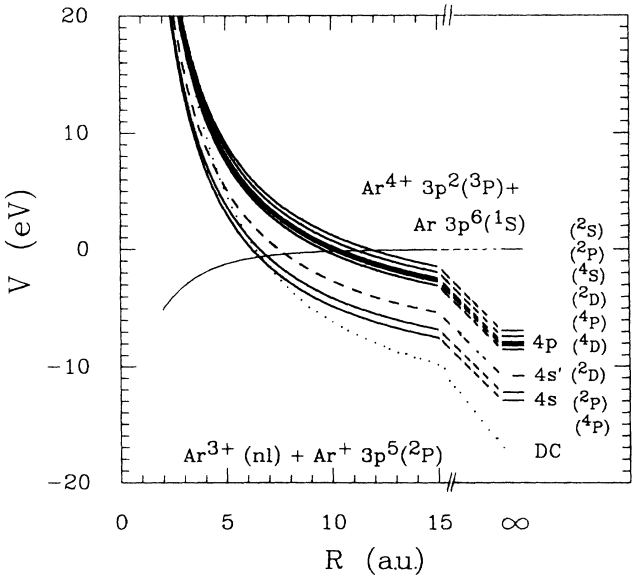

FIG. 3. A potential-energy diagram for the Ar^{4+}-Ar system. The potential-energy curves of the incoming channel and single- and double-electron-capture exiting channels are plotted as functions of the internuclear distance R. The incoming potential includes polarization of the target, damped at small R (cf. text). The single-capture potentials include Coulomb repulsion and the polarization energy (with the same damping function as the incident channel) of the Ar^+ ground-state ion. A pure Coulomb double-capture potential curve (dotted) is inserted at the experimentally established Q value of 17 eV. Six $4p$ and two $4s$ terms, added to the ground-state ^3P term in Ar^{4+}, correspond to single-capture potentials, indicated by solid curves. The dashed curve shows a potential that dissociates to the ground-state Ar^+ ion and the $4s\ ^2D$ Ar^{3+} term, denoted by $4s'$. The latter is built on the excited Ar^{4+} (^1D) core.

$$\frac{d\sigma_{0k}}{d\Omega}=\sum_j P_k^{(j)}\frac{d\sigma_{0k}^{(j)}}{d\Omega} +2\sum_j\sum_{i\,(>j)}\left[P_k^{(j)}P_k^{(i)}\frac{d\sigma_{0k}^{(j)}}{d\Omega}\frac{d\sigma_{0k}^{(i)}}{d\Omega}\right]^{1/2} \times\cos(A_k^{(j)}-A_k^{(i)})\ . \quad (8)$$

The interference phases $A_k^{(j)}-A_k^{(i)}$ are related to the areas between the branches of the classical deflection function[38] corresponding to paths j and i. We refrain from including any quantum corrections to the semiclassical phases $A_k^{(j)}$ of the scattering amplitudes $f_{0k}^{(j)}$ at this level of sophistication. As a consequence, the oscillatory pattern in Eq. (8) may be shifted compared to the true pattern (see, e.g., Koslowski *et al.*[39]). The oscillation frequencies will, however, be the same.

Another modification of the original version of the model by Andersson *et al.*[36] concerns the diabatic coupling element that enters in Eq. (6). For collisions between completely stripped ions and atomic hydrogen, Olson and Salop[26] derived the semiempirical expression

$$H_{12}^{\rm OS}=9.13q^{-1/2}\exp[-1.324q^{-1/2}(2I_t)^{1/2}R_x]\ , \quad (9)$$

where I_t is the ionization potential of the target and R_x is the crossing radius. The dependence on I_t was introduced to allow for targets with ionization potentials different from $\frac{1}{2}$. Different modifications of $H_{12}^{\rm OS}$ have been suggested in the literature. Kimura *et al.*[40] reduced $H_{12}^{\rm OS}$ by 40% to fit their experimental data and Taulbjerg[27] derived a correction factor F_{nl} that depends on the final capture state. We note that $H_{12}^{\rm OS}$ and the correction factor F_{nl} have proven reasonably accurate for capture to a projectile initially in an S state.[27,36] For a more general collision system with an open-shell core on the projectile, the capture into a given (n,l) level of the projectile will result in several LS terms. The wave function of the final projectile state has angular momentum properties that influence its coupling to the initial state. The rigorous selection rules for radial coupling are conservation of the projections of the total orbital and spin angular momenta on the internuclear axis. In an independent-particle model the selection rules apply to the same constants of motion for individual electrons. We adopt the point of view that an independent-particle model is sufficient at distant crossings while electron correlation is important for determining the asymptotic energies.

In the present system all possible LS terms ($3p^2\,{}^3P\ 4l\ {}^{2S+1}L$) for capture to the $l=0,1$ levels formed on the Ar^{3+} projectile in the final channels are allowed to couple to the incident channel. However, only the parts of the initial and final wave functions that contain the active electron with the same projections of orbital and spin angular momenta on the internuclear axis are allowed to couple, due to the assumption of radial spin-independent coupling. Moreover, since the target has six valence electrons, we must allow for the fact that these are indistinguishable and equally probable to play the role of the active electron.

To determine the diabatic couplings we use here a version of a procedure originally suggested by Grice and Herschbach[41] for neutral collision systems and more recently used for ion-atom collision systems by Gargaud and McCarroll.[42] The objective of this procedure is to reduce the matrix element of the electronic Hamiltonian $H_{\rm el}$ between two multielectron diabatic states to a one-electron matrix element between the initial and final states of the active electron. For distant crossings a diabatic state of the quasimolecule can be reasonably approximated by linear combinations of atomic orbitals (LCAO's) of the dissociation products to which the diabatic state correlates. In the interaction region we describe the atomic systems by single-configuration LS-coupled spin orbitals. These do not, of course, give the correct energies in the asymptotic region. We label the orbitals by their atomic dissociation limit rather than using molecular notation. This is permissible at large internuclear separations where mixing of the orbitals on different centers is negligible. In the initial channel the Ar target is in the state (subscript B denotes the target center)

$$|i\rangle_B=|3p^6\,{}^1S,0,0\rangle_B =\sum_{m_1,m_2}\sum_{\mu_1,\mu_2}\begin{pmatrix}1&1&0\\m_1&m_2&0\end{pmatrix}\begin{pmatrix}\frac{1}{2}&\frac{1}{2}&0\\\mu_1&\mu_2&0\end{pmatrix} \times|3p^5\,{}^2P^o,m_1,\mu_1\rangle_B \otimes|3p,m_2,\mu_2\rangle_B\ , \quad (10)$$

where

$$\begin{pmatrix}j_1&j_2&J\\m_1&m_2&M\end{pmatrix}$$

denote the Clebsch-Gordan coefficients and m_i and μ_i are the projection quantum numbers of the orbital angular momentum and the spin, respectively. The state of Eq. (10) is antisymmetric in the six $3p$ electrons if $|3p^5\,{}^2P,m_1,\mu_1\rangle_B$ is properly antisymmetrized. The single-electron state that is explicitly singled out in Eq. (10) will describe the active electron.

The Ar^{4+} projectile (center A) is in the state

$$|i\rangle_A=|3p^2\,{}^3P,m_i,\mu_i\rangle_A\ . \quad (11)$$

The LCAO's that describe the initial states are formed using Eqs. (10) and (11):

$$|i,{}^3|\Lambda|,\Lambda,\mu\rangle=|3p^2\,{}^3P,\Lambda,\mu\rangle_A\otimes|3p^6\,{}^1S,0,0\rangle_B\ . \quad (12)$$

The states in Eq. (12) are eigenstates of the orbital angular momentum operator L_z along the internuclear axis (z axis) with eigenvalues Λ. Alternatively, we could choose eigenstates of the reflection operator σ_v, which reflects the spatial part of the wave function in a plane containing the z axis. For $\Lambda=0$, Eq. (12) is a simultaneous eigenstate of L_z and σ_v. The reflection symmetry for a molecular state is the same as for the atomic states to which the molecular state dissociates. For an atomic angular momentum eigenstate $|L,M,\pi\rangle$, where π is $+1$ for an

TABLE I. The possible molecular terms obtained from combining the atomic states in Eqs. (14) and (15). l is the angular momentum of the captured electron, S_A and L_A the total spin and orbital angular momentum of the projectile, S total spin of the molecular term, and Λ the orbital angular momentum component along the molecular axis. The numbers in parentheses denote the number of this type of term. The degeneracy of the $\Lambda \neq 0$ terms due to the two possible signs of Λ is implicitly understood.

l	$^{2S_A+1}L_A$	$^{2S+1}\lvert\Lambda\rvert$				
0	^2P	$^{1,3}\Sigma^-(2)$	$^{1,3}\Sigma^+$	$^{1,3}\Pi(2)$	$^{1,3}\Delta$	
0	^4P	$^{3,5}\Sigma^-(2)$	$^{3,5}\Sigma^+$	$^{3,5}\Pi(2)$	$^{3,5}\Delta$	
1	$^2S^o$	$^{1,3}\Sigma^-$		$^{1,3}\Pi$		
1	$^4S^o$	$^{3,5}\Sigma^-$		$^{3,5}\Pi$		
1	$^2P^o$	$^{1,3}\Sigma^-$	$^{1,3}\Sigma^+(2)$	$^{1,3}\Pi(2)$	$^{1,3}\Delta$	
1	$^4P^o$	$^{3,5}\Sigma^-$	$^{3,5}\Sigma^+(2)$	$^{3,5}\Pi(2)$	$^{3,5}\Delta$	
1	$^2D^o$	$^{1,3}\Sigma^-(2)$	$^{1,3}\Sigma^+$	$^{1,3}\Pi(3)$	$^{1,3}\Delta(2)$	$^{1,3}\Phi$
1	$^4D^o$	$^{3,5}\Sigma^-(2)$	$^{3,5}\Sigma^+$	$^{3,5}\Pi(3)$	$^{3,5}\Delta(2)$	$^{3,5}\Phi$

even state and π is -1 for an odd state, the reflection operation has the effect

$$\sigma_v|L,M,\pi\rangle=\pi(-1)^{L+M}|L,-M,\pi\rangle \ . \tag{13}$$

Using Eq. (13), one can deduce that the initial molecular states in Eq. (12) are one $^3\Sigma^-$ state and one (doubly degenerate) $^3\Pi$ state.

For the final channels the atomic states are

$$|f\rangle_B=|3p^5\,{}^2P^o,m_B,\mu_B\rangle_B \tag{14}$$

for ground-state Ar^+ and

$$|f\rangle_A=|3p^2\,{}^3P\ 4l\ {}^{2S_A+1}L_A,m_A,\mu_A\rangle_A = \sum_{m_1,m_2}\sum_{\mu_1,\mu_2}\begin{bmatrix}1 & l & L_A\\ m_1 & m_2 & m_A\end{bmatrix}\begin{bmatrix}1 & \frac{1}{2} & S_A\\ \mu_1 & \mu_2 & \mu_A\end{bmatrix} \times|3p^2\,{}^3P,m_1,\mu_1\rangle_A \otimes|4l,m_2,\mu_2\rangle_A \tag{15}$$

for Ar^{3+}. The combination of the atomic states in Eqs. (14) and (15) will give rise to the molecular terms listed in Table I. The figures in parentheses after some terms denote the number of this type of term if different from one. All terms with $\Lambda\neq0$ are doubly degenerate due to the two possible signs of Λ.

The general final molecular state is written

$$|f,4l\ {}^{2S_A+1}L_A;{}^{2S+1}|\Lambda|,\Lambda,\mu\rangle =(6)^{-1/2}\hat{A}\sum_{\mu_1,\mu_2}\begin{bmatrix}S_A & \frac{1}{2} & S\\ \mu_1 & \mu_2 & \mu\end{bmatrix}\sum_{M=-1}^{1}K_M|3p^2\,{}^3P\ 4l\ {}^{2S_A+1}L_A,\Lambda-M,\mu_1\rangle_A\otimes|3p^5\,{}^2P^o,M,\mu_2\rangle_B \ , \tag{16}$$

where K_M are coefficients that decide the reflection properties of the Σ terms [by using Eq. (13)] and ensure normalization. The states in Eq. (16) are constructed to be eigenstates of L_z with eigenvalues Λ. In Eq. (16) $\hat{A}$ is the operator that antisymmetrizes the transferred electron with the five $3p$ electrons remaining on the target. The final state in Eq. (16) must be antisymmetric in these electron coordinates to be consistent with the initial state in Eq. (12). Since the two ionic cores are identical, we should, of course, also distinguish between gerade and ungerade states. For the present considerations, however, this is not necessary because we have excluded the symmetric charge-transfer channel ($Ar^{4+}+Ar\rightarrow Ar+Ar^{4+}$) where this distinction is important.

The matrix element of H_{el} between the initial state $|i,{}^3|\Lambda|,\Lambda,\mu\rangle$ and the final state

$$|f,4l\ {}^{2S_A+1}L_A,\ {}^{2S+1}|\Lambda'|,\Lambda',\mu'\rangle$$

at their crossing radius can, provided that the overlap ${}_A\langle4l|3p\rangle_B$ is small compared to unity, be written[41,42]

$$H_{fi}=g_Lg_S\,{}_A\langle4l|\,|H_{el}|\,|3p\rangle_B \ , \tag{17}$$

where

$$g_L=\sum_{M=-1}^{1}K_M\begin{bmatrix}1 & l & L_A\\ \Lambda & M & \Lambda-M\end{bmatrix}\begin{bmatrix}1 & 1 & 0\\ M & -M & 0\end{bmatrix}\delta_{\Lambda,\Lambda'} \tag{18}$$

and

$$g_S=\sqrt{6}\sum_m\begin{bmatrix}\frac{1}{2} & \frac{1}{2} & 0\\ m & -m & 0\end{bmatrix}\begin{bmatrix}1 & \frac{1}{2} & S_A\\ \mu & -m & \mu-m\end{bmatrix} \times\begin{bmatrix}S_A & \frac{1}{2} & S\\ \mu-m & m & \mu\end{bmatrix}\delta_{\mu,\mu'} \ . \tag{19}$$

In deriving Eqs. (18) and (19), we have used the fact that each electron must conserve its projections of orbital and spin angular momenta on the z axis separately. The one-electron matrix element remaining in Eq. (17) does not involve integration over the azimuthal angle since this has been trivially performed by the angular momentum selection rules.

In order to determine the factors g_L, the coefficients K_M must be known. If a molecular term only occurs once, this presents no difficulty since reflection properties and normalization fix the values (up to a common phase factor). The terms that occur more than once (cf. Table I) are, in general, split in energy depending on the electronic configuration. At the relevant internuclear separations, however, this splitting is expected to be negligible and we regard the terms to be effectively degenerate. In that case, the K_M's for each of those terms can be chosen freely as long as orthonormalization is satisfied. This will, in general, lead to several different values of g_L. Since in this Landau-Zener curve-crossing model all interaction between the initial and the final channel is mediated by H_{fi} localized at the curve crossing, the values of the (in principle, R-dependent) coefficients K_M are important only at the curve-crossing radius. By choosing the K_M's in such a way that the g_L's are zero for all but one of the degenerate states, the ambiguity of the g_L's is resolved. In this way the coupling mechanism determines, at the curve crossing, a particular LCAO to represent a given molecular term. It is also crucial that each final state interacts only with the initial state and not with the other final states.

In Table II we give the values of g_S and in Table III the nonzero values of g_L together with the corresponding values of the K_M's. It is understood in Table III that the $\Lambda=0$ states are Σ^- states since $g_L=0$ for the Σ^+ states. It can be noted from Table II that only the final triplet channels couple to the initial channel (which is always a triplet) in accordance with Wigner's $\Delta S=0$ spin-selection rule.

The one-electron matrix element ${}_A\langle 4l|\,|H_{\rm el}|\,|3p\rangle_B$ in Eq. (17) could, of course, be calculated by some one-electron model, as was done by Gargaud and McCarroll.[42] We here choose a much simpler approach and use $H_{12}^{\rm OS}$ given by Eq. (9) corrected by Taulbjerg's factor[27] F_{nl}. We thus have

$$H_{fi}=g_L g_S F_{nl} H_{12}^{\rm OS} \ . \tag{20}$$

This particular choice cannot be strictly justified, however; since $H_{12}^{\rm OS}$ describes capture from a target with a given ionization potential to hydrogenic levels of a one-electron ion and F_{nl} accounts for the splitting of the l levels for an ion having a core, it seems reasonable to use $F_{nl}H_{12}^{\rm OS}$ for the one-electron element. The results obtained in this work also give *a posteriori* justification for using the couplings in Eq. (20).

Since differential cross sections for double capture have been recorded, we also extend the collision model by inclusion of one double-capture channel represented by the diagonal diabatic state

$$V_{\rm DC}(R)=\frac{2(q-2)}{R}-Q_{\rm DC} \ . \tag{21}$$

The purpose is to investigate the influence of the double-capture channel on the angular distributions for single-electron capture [according to Eqs. (4) and (5) without the penetration term] and to check the experimental data for one- or two-step double capture. $V_{\rm DC}$ will cross the initial channel V_0 at $R=R_{\rm DC}^0$ and the final single-capture channels V_k at $R=R_{\rm DC}^k$. In order to investigate the influence from double-capture channels on the single-capture angular distributions, we allow transitions at

TABLE II. Values of g_S given by Eq. (19). S_A is the spin of the final projectile state and S the spin of the molecular state.

S_A	S	g_S
$\frac{1}{2}$	0	0
$\frac{1}{2}$	1	$\sqrt{2}$
$\frac{3}{2}$	1	2
$\frac{3}{2}$	2	0

TABLE III. The nonzero values of g_L given by Eq. (18). l is the orbital angular momentum of the captured electron, L_A is the total orbital angular momentum of the projectile, and Λ the orbital angular momentum projection on the internuclear axis of the molecular term. K_M are the coefficients for building the final-state molecular LCAO [cf. Eq. (16)]. $\Lambda=0$ denotes Σ^- states; Σ^+ states have $g_L=0$.

l	L_A	Λ	g_L	K_0	K_1	K_{-1}
0	1	0	$1/\sqrt{3}$	1	0	0
0	1	1	$1/\sqrt{3}$	1	0	0
1	0	0	$\frac{1}{3}$	1	0	0
1	0	1	$\frac{1}{3}$	0	1	0
1	1	0	$1/\sqrt{3}$	0	$1/\sqrt{2}$	$-1/\sqrt{2}$
1	1	1	$1/\sqrt{3}$	$1/\sqrt{2}$	$-1/\sqrt{2}$	0
1	2	0	$\sqrt{5}/3$	$\sqrt{2/5}$	$-\sqrt{3/10}$	$-\sqrt{3/10}$
1	2	1	$\sqrt{5}/3$	$\sqrt{3/10}$	$-\sqrt{1/10}$	$-\sqrt{3/5}$

R^k_{DC} but not at R^0_{DC}. In other words, double capture is allowed to take place via two-step processes where one electron is captured at the crossing between the initial channel and the single-capture channel V_k and subsequently the other electron is captured at R^k_{DC}. In order to keep the MCLZ expressions simple, we do not allow for coupling between different single-capture channels via the double-capture channel. This is clearly inconsistent but sufficient for our purposes, since the primary interest is to determine principal features of the angular distribution. The coupling matrix elements between the single- and double-capture channels are kept as free parameters which are adjusted to give a substantial probability for populating the double-capture channel. As can be seen below, the double-capture channel has negligible influence on the single-capture differential cross sections at angles detected by the experiment. This justifies a calculation for single capture that disregards the presence of double-capture channels. In order to investigate the second point, the coupling at R^0_{DC} is switched on, allowing for simultaneous transfer of two electrons. As expected, and as will be discussed in more detail in Sec. IV B, the scattering angles are smaller for this transition than for the two-step process because a larger portion of the slightly attractive initial channel is traversed before switching to the repulsive double-capture channel.

IV. RESULTS AND DISCUSSIONS

A. Single-electron capture

Energy-gain spectra for forward-scattered ($\theta < 1°$) Ar^{4+}-Ar single-electron capture, and the Q values associated with the $4p$ and $4s$ terms and a term denoted by $4s'$, are shown in Fig. 4. The $4p$ and $4s$ terms are all built on the ^3P Ar^{4+} ground state while the $4s'$ term is built on the excited ^1D Ar^{4+} core. The exclusive population of the $4p$ states in the laboratory energy range 19–200 eV is evident from the positions of single peaks at $\Delta E \sim 8.5$ eV, where we estimate the uncertainty in the absolute calibration of the energy-gain scales to be ± 0.5 eV. The relative energy resolution of the setup with the cylindrical energy analyzer is about 1.6%, while the relative energy widths of the single-capture peaks vary from 6.6% for the lowest energy down to 2.2% for 200 eV. The six unresolved $4p$ LS terms, distributed over excitation energies of 1.6 eV and with separations between 0.1 and 0.5 eV, presumably make up the main part of this extra broadening. At 19 eV, the measured absolute peak width of 1.85 eV is dominated by the distribution of capture of the $4p$ $^2S^o$, $^2P^o$, $^4S^o$, $^2D^o$, $^4P^o$, and $^4D^o$ levels, with a somewhat smaller contribution from the energy spread of ~ 0.8 eV for the incident Ar^{4+} beam.

The dominance of single-electron capture to the $4p$ state in the energy range below 200 eV is in accordance with earlier experimental results. Puerta *et al.*[18] and Koslowski and Huber[19] recorded one order of magnitude more intensity in the $4p$ than in the $4s$ state by means of translational energy-gain spectroscopy for Ar^{4+}-Ar collisions at 800 eV. At 2180 eV Giese *et al.*[17] noted that $4p$ capture is twice as probable as capture to the $4s$ state. In unpublished measurements for the same collision system, Hvelplund and Cederquist[20] recorded a decreasing relative importance of $4s$ capture as the collision energy was lowered. At 240 eV a relative cross section of a few percent was measured, while only $4p$ capture could be detected at their lowest energy of 160 eV. This energy variation of the $4s$ capture cross section strongly indicates that the avoided crossing between the outermost $4s$ channel (^2P) and the incident channel is passed adiabatically in the energy regime below 200 eV.

The energy-gain spectra of Fig. 4 show that there is no population of the $4s'$ term (^1D $4s$ ^2D) expected at $Q = 10.8$ eV, at least not in the energy range 19–200 eV. At higher energies, the limited resolution excludes the detection of possible minor contributions. There is, however, no trace of population of this channel in the data of Puer-

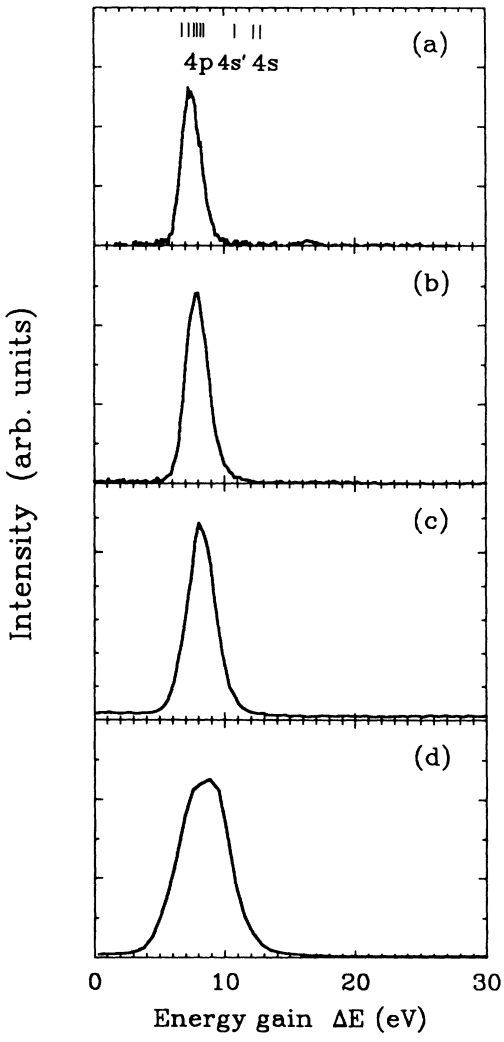

FIG. 4. Energy-gain spectra for single-electron capture within projectile scattering angles of $\pm 1°$ in Ar^{4+}-Ar collisions at (a) 19, (b) 40, (c) 80, and (d) 200 eV. The energies for capture to $4s$, $4s'$ (cf. text), and $4p$ states are indicated.

ta *et al.*[18] or Koslowski and Huber[19] at 800 eV. Also the data by Hvelplund and Cederquist[20] at several points in the energy range 160–600 eV demonstrate the absence of this feature. It is thus clear that the crossing between the incident and the $4s'$ channel is either strongly adiabatic or strongly diabatic over the whole present energy range of 19–800 eV. An adiabatic behavior of the crossing with the $4s'$ channel would involve an excitation of the ^3P Ar^{4+} core and a simultaneous electron transfer. It is shown in numerous experiments that transfer-excitation processes, which proceed through similar couplings, occur at smaller internuclear separations than core-preserving single-electron capture.[43] Furthermore, given a diabatic transition probability at the $4s'$ crossing of either zero or one, the population of $4s$ in the upper part of the present collision-energy regime strongly suggests a diabatic behavior for this crossing, since a complete adiabaticity does not allow capture to channels of smaller crossing distances.

Before we proceed with the comparison between model and experimental angular distributions, a discussion on the possibility of metastable components in the projectile beam is appropriate. Puerta *et al.*[18] did indeed detect capture to the $^2D^o$ and $^2P^o$ levels of Ar^{3+} at Q values close to 10 eV in 800-eV collisions on Ar. The population of these levels, at this Q value, is unambiguously identified as capture to a $4p$ state by an incoming ^1D Ar^{4+} metastable core.[18] The same feature is also seen in the spectrum reported by Koslowski and Huber.[19] A contamination by ^1D metastables should have the same signature in the present energy-gain spectra, but at least for energies below 80 eV where a peak from this process would be resolved, no such contribution is detected. In this context one should note that our considerably lower collision energies tend to decrease the probability for capture to states of large Q values, which is clearly demonstrated by the energy dependence of reaction windows presented by Biedermann *et al.*[10] There are two Ar^{3+} LS terms based on the ^1D core that give Q values in the near vicinity of $Q=8.5$ eV. Thus, it cannot be excluded that capture to this metastable core contributes to the peaks in Fig. 4. The remaining metastable Ar^{4+} component, ^1S, does not provide crossings within the reaction window for Ar^{4+}-Ar collisions and is not expected to affect the energy-gain spectra at 800 eV or below.[18] We cannot rule out the possibility of ^1D metastable contamination in the $4p$ single-capture states, but since they occur at roughly the same Q value and thereby cross the incident channel at about the same R, the projectile deflection will be the same for a given path on the internuclear potentials. The coupling strengths might, however, differ due to the differences in angular properties for the incoming ground- and metastable-state wave functions. In concluding the discussion about metastable beam components, we note that a possible presence of ^1S Ar^{4+} projectiles would affect only the magnitude of the apparent total experimental single-capture cross section. A ^1D Ar^{4+} beam component, however, may contribute to single-electron capture and would exhibit the same angular distribution as the ^3P ground-state projectile but with a different relative intensity distribution.

Comparisons between experimental and theoretical results for the angular distributions of single-electron capture to the $4p$ state of Ar^{3+} are shown for several collision energies in Fig. 5. In the calculations, we assume all six $4p$ channels to be open. We take the innermost of the two $4s$ channels ($4s\ ^4P$) as the inner repulsive wall, i.e., we have assumed that it is completely adiabatic. The outer $4s$ channel ($4s\ ^2P$), left open in the calculations, yields in very small diabatic transition probabilities for the corresponding crossing at energies below 200 eV. Thus this channel in effect acts as a repulsive wall. The

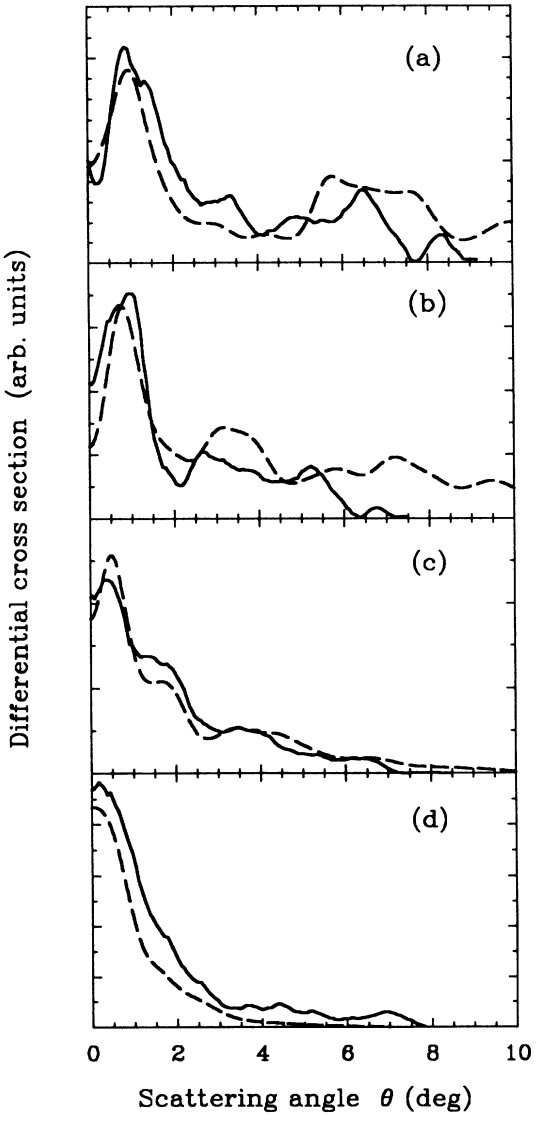

FIG. 5. Comparisons between the experimental (solid lines) and calculated (dashed lines) angular distributions for single-electron capture to the Ar^{3+} $4p$ state in Ar^{4+}-Ar collisions at (a) 19, (b) 40, (c) 80, and (d) 200 eV. The theoretical results (dashed lines) are $d\sigma/d\Omega$, convoluted with the experimental angular resolution, and include interference effects.

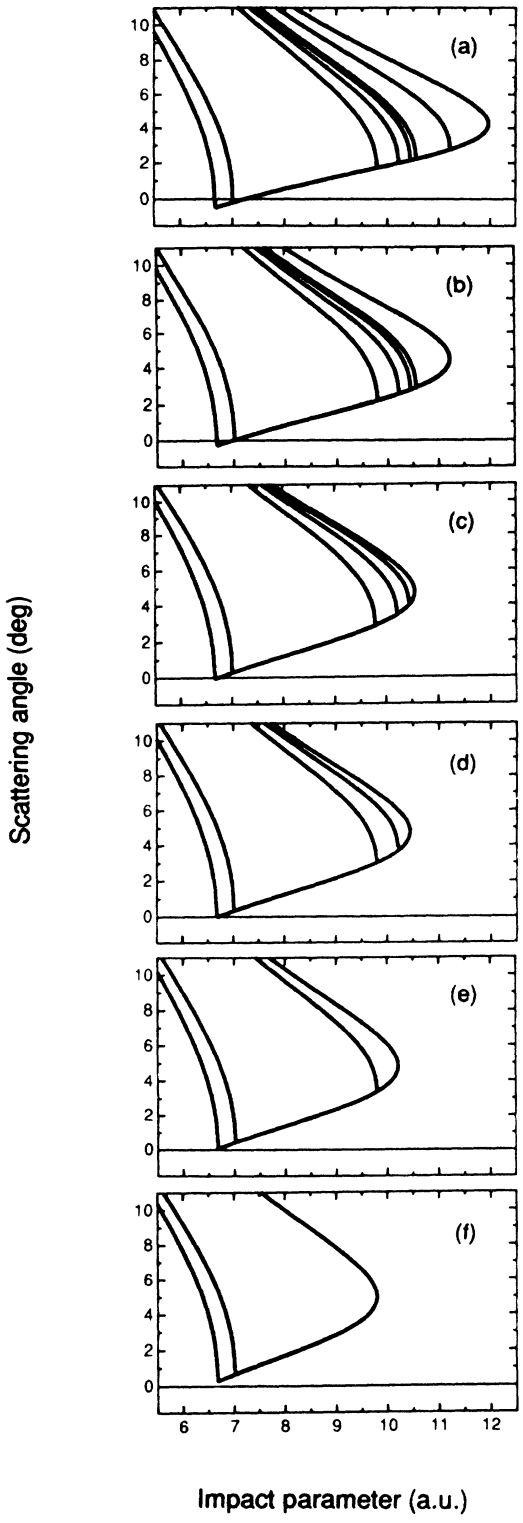

FIG. 6. The laboratory deflection functions for the processes $Ar^{4+}\ 3p^2\ (^3P^e) + Ar\ 3p^6\ (^1S^e) \rightarrow Ar^{3+}\ 3p^2\ 4p\ (^{2S+1}L^o) + Ar^+\ 3p^5\ (^2P^o)$, at the laboratory collision energy 40 eV. The projectile scattering angle θ is shown as a function of the impact parameter b. From top to bottom the (a) $^2S^o$, (b) $^2P^o$, (c) $^4S^o$, (d) $^2D^o$, (e) $^4P^o$, and (f) $^4D^o$ deflection functions are shown in decreasing order of the distance for the corresponding $4p$ channel crossing with the incident channel.

coupling to the $4s'$ channel is assumed to be negligibly weak and we further assume that the incoming Ar^{4+} projectile is in the ground state. For each of the $4p$ exit channels a deflection function is calculated by numerical

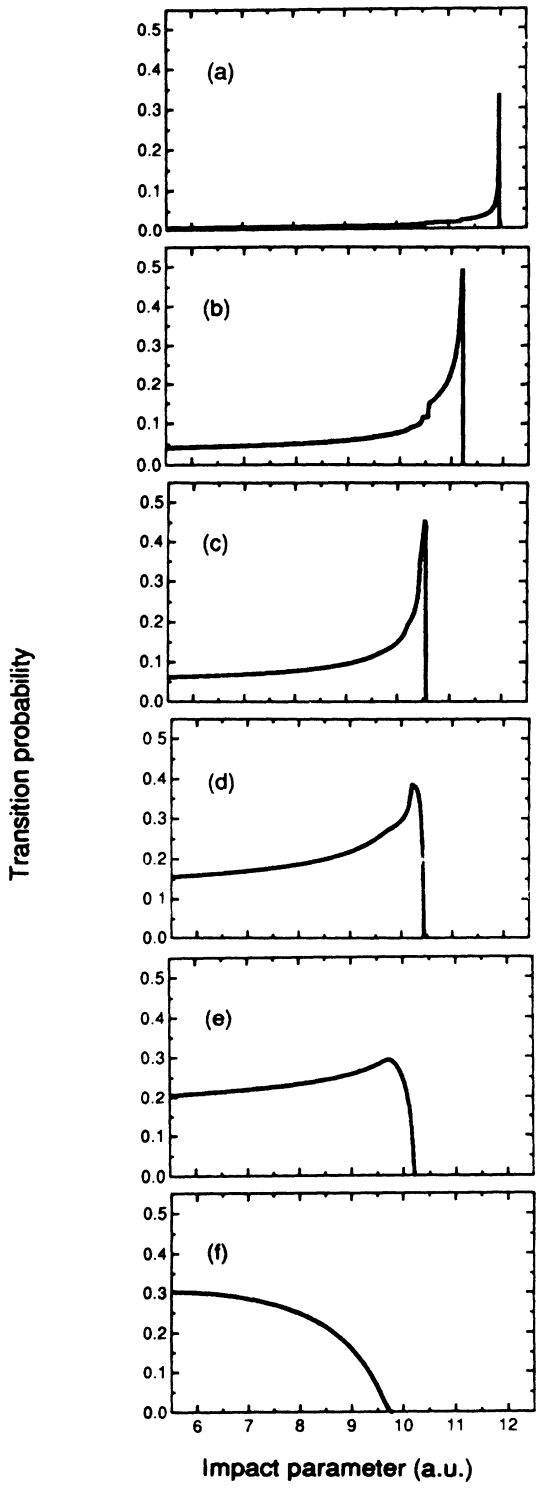

FIG. 7. The multichannel Landau-Zener probabilities $P(b)$ to populate the $4p$ (a) $^2S^o$, (b) $^2P^o$, (c) $^4S^o$, (d) $^2D^o$, (e) $^4P^o$, and (f) $^4D^o$ single-electron-capture channels, as functions of the impact parameter b, in 40-eV Ar^{4+}-Ar collisions.

integration along the incident, $4p$, and $4s$ paths on the diabatic potentials of Fig. 3. These deflection functions are shown for the laboratory collision energy of 40 eV in Fig. 6. The probability flux on the different branches of each deflection function are calculated by the use of the diabatic coupling elements of Sec. III, which take the angular momentum selection rules into account. Coherent addition of the scattering amplitudes associated with these branches yields to $d\sigma/d\Omega$ for each particular final $4p$ LS term. The total angular differential cross section for capture to the $4p$ state is then obtained by incoherent addition of the contributions from the six $4p$ LS channels. In Fig. 7, the multichannel Landau-Zener transition probabilities $P(b)$ are shown as functions of the impact parameter b for the six exiting $4p$ LS terms. The partial and the summed angular differential cross sections, $d\sigma/d\Omega$, for 40-eV Ar^{4+}-Ar collisions are shown in Fig. 8. In contrast to the angular distribution in Fig. 5, the ones in Fig. 8 do not include interference effects. As we will show below, Stueckelberg oscillations only have a limited influence on the total $4p$ angular differential cross sections.

The experimental data shown in Fig. 5 were obtained with the 30° parallel-plate electrostatic analyzer, which gives slightly better angular resolution than the cylindrical analyzer. The theoretical cross sections $d\sigma/d\Omega$ follow the measured angular distributions closely for the energies 19, 40, 80, and 200 eV. For more energetic collisions, both calculations and measurements yield in a single forward peak. As has been mentioned above, the single parameter (λ) in the present calculation is set by requiring agreement for the peak closest to 0° for all of the collision energies of Fig. 5. The positions and the magnitudes of these primary peaks are very sensitive to the shape of the incident channel, since this affects the minimum angles of the six deflection functions. The inclusion of the polarization energy term in this potential is necessary in order to obtain a primary peak in the model this close to the forward direction at the lowest energies. This polarization energy term and the terms added to the Coulomb potential of the outgoing single-capture channels are all multiplied by the same function $[1-\exp(-\lambda R)]^4$. A deviation of a few percent in λ makes a significant difference and we arrive at $\lambda=0.28$. In contrast, as we will show below, the model angular distributions outside the primary peaks are extremely insensitive to the shape of the incident channel.

According to the calculations, the forward peaks in the energy range below 200 eV are dominated by rainbow scattering due to the adiabaticity of the $4s$ ^2P channel. From the calculated distributions for 40 eV, shown in Fig. 8, we note that the positions of the forward rainbows are different for the different $4p$ exiting channels. As the collision energy is increased, this difference is diminished, but at 19 eV a feature caused by the forward rainbow of the innermost $4p$ channel appears on the large-angle side of the primary peak and in the vicinity of $\theta=3°$ [cf. Fig. 5(a)]. Secondary intensity maxima are present at about 1.8° for 80 eV collision energy and at ~3.5° and ~6.5° for 40 and 19 eV, respectively. It is evident from the partial $4p$ cross sections for 40-eV Ar^{4+}-Ar collisions (Fig.

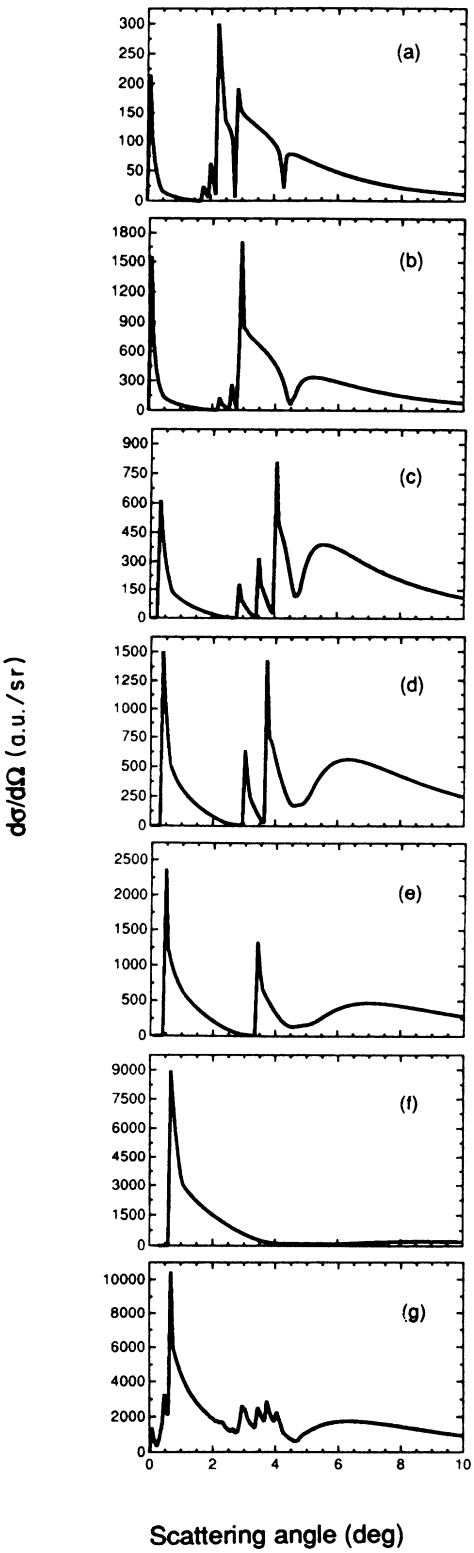

FIG. 8. Angular differential cross sections for single-electron capture to the six $4p$ ^{2S+1}L levels of Ar^{3+} [in order of (a) $^2S^o$, (b) $^2P^o$, (c) $^4S^o$, (d) $^2D^o$, (e) $^4P^o$, and (f) $^4D^o$ from the top] in 40-eV Ar^{4+}-Ar collisions. At the bottom, the sum of all six cross sections is shown (g). Note the differences in intensities and vertical scales for the different partial $4p$ cross sections.

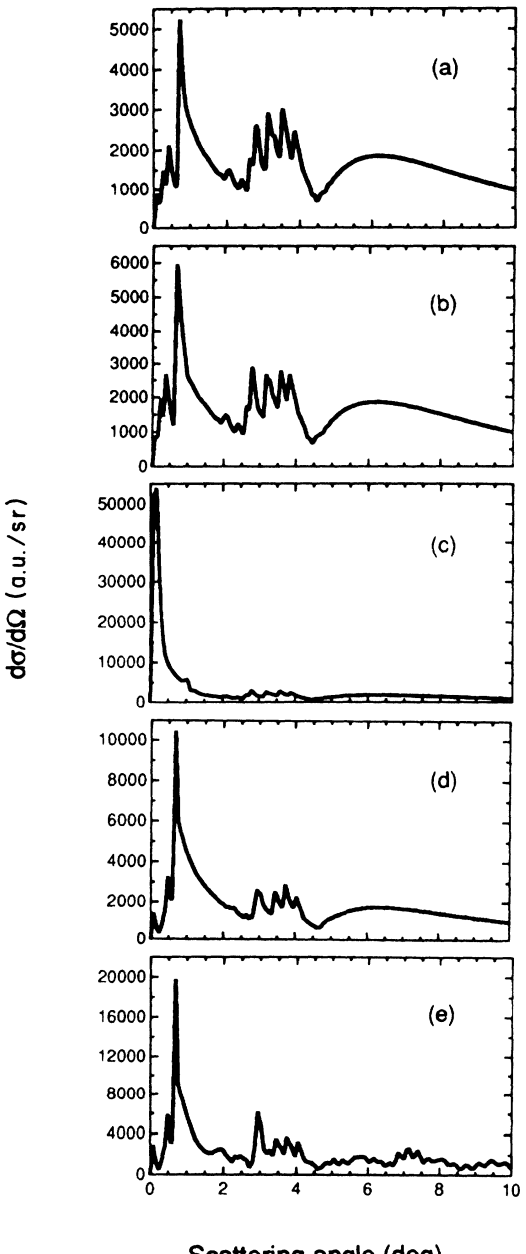

FIG. 9. Calculations of angular differential cross section for 40-eV $Ar^{4+}+Ar \rightarrow Ar^{3+}$ $(4p)+Ar^{+}$ under different assumptions for the interatomic potentials. The core-excited (^1D) $4s\,^2D$ Ar^{3+} single-capture channel $(4s')$ is assumed to be completely adiabatic in the (a) calculation, which includes polarization and core penetration in the initial and final channels. The calculation resulting in the angular differential cross section shown in (b) is the same as in (a) except that core penetration is excluded. In (c), polarization is included and the crossing with the core-excited $4s'$ single-capture state is assumed to be diabatic with the $4s\,^4P$ curve as the repulsive wall. In (d) potentials are as in (c), except that the polarization energies in the initial and final channels are damped at small R (cf. text). The calculation for (e) is the same as the one for (d), except that interferences between intensities on different branches of the multivalued deflection functions are introduced.

8), and the ones for 19 and 80 eV (not shown), that this secondary structure is due to rainbow scattering associated with the branches of the deflection functions that correspond to $4p$ channels inside the ones finally populated. All partial $4p$ cross sections contribute to this peak except the one in which the innermost of the $4p$ LS terms is populated. The existence of such secondary intensity maxima is also evident in the data on single-electron capture in Ar^{4+}-Ar collisions at 88, 68, 53, and 33 eV which were presented before.[9] The intensities at angles outside the secondary peaks are due to transfer to the final $4p$ channel on the way into the collision, i.e., they are associated with the outermost branches of the six deflection functions. Note that there are small shifts also between the secondary rainbow angles, due to the slight differences between deflection functions for the six exiting $4p$ channels (cf. Fig. 8). The calculated angular distributions are very sensitive to the magnitudes of the matrix elements at the avoided crossings and the present agreement between model and experimental results supports the suggested reduction due to the angular momentum selection rules. Without this reduction, the forward peaks of the calculated distributions would shift greatly in angle and magnitude regardless of the numerical value of the parameter λ.

Calculated angular differential cross sections for single-electron capture to the $4p$ state of Ar^{3+} are shown in Fig. 9 for different assumptions about the interatomic potentials. In Figs. 9(a) and 9(b) the coupling to the $4s'$ channel is assumed to be completely adiabatic and the undamped polarization potentials of Ar and Ar^{+} are included.[10] The potential energies associated with the projectile's penetration of the outermost electron shells of Ar and Ar^{+}, included in Fig. 9(a) but not in Fig. 9(b), obviously have negligible effects on $d\sigma/d\Omega$. In Figs. 9(c), 9(d), and 9(e), polarization energies are included, and it is assumed that the $4s'$ channel is passed diabatically in the collision. Note the differences in scales and primary peak positions between Fig. 9(c) and Fig. 9(d) which is due to the damping function applied to the polarization terms in Fig. 9(d). The calculation giving the angular differential cross section displayed in Fig. 9(e) is identical to the one in Fig. 9(d) except that the interference effects (discussed in Sec. III) are taken into account. The Stueckelberg oscillations do indeed have drastic influences on the six partial $4p$ LS angular distributions, but by the incoherent addition of these most of the interference structure is smeared out. When the results are convoluted with the experimental response function, the effect of including Stueckelberg oscillations is even harder to detect. In Fig. 10, comparisons between convoluted angular differential cross sections with and without interference effects are shown for the energies 19, 40, 80, and 200 eV. Finally, note that the absolute intensity of the secondary peak at $\theta \sim 3°$ is insensitive to the different assumptions presented in Fig. 9. Thus our conclusion that the secondary structures in the angular distributions are due to rainbow scattering associated with the existence of several close lying $4p$ LS exiting channels is indeed insensitive to the shape of the incoming potential and even to the position of the inner repulsive wall.

As will be discussed below, we have made calculations for the angular scattering in two-electron capture in Ar^{4+}-Ar collisions. In principle, it is possible that double-capture channels might influence the single-capture angular distribution. For example, a higher-order transition from the $4p$ level to the double-capture level on the way into the collision could occur, followed by a transition to one of the $4p$ levels on the way out. We have included a hypothetical double-capture channel at $Q=17$ eV, which is the experimentally determined value, in order to investigate this matter. This channel introduces extra branches, at larger angles, starting in the impact-parameter region around 4 to 5 a.u. on all the $4p$ single-capture branches of the deflection functions. For

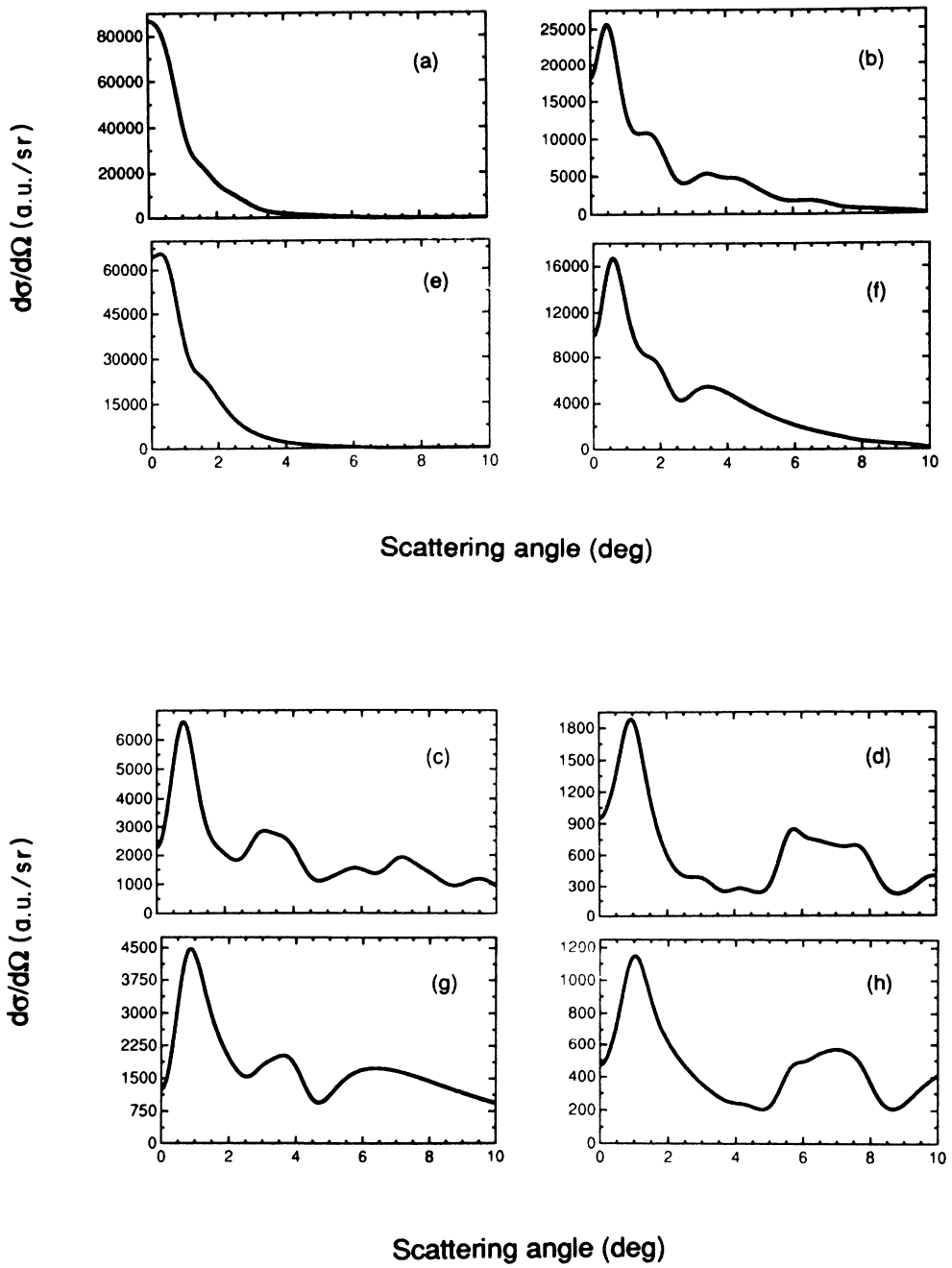

FIG. 10. Calculations of angular differential cross sections for capture to the $4p$ state of Ar^{3+} in Ar^{4+}-Ar collisions at [(a) and (e)] 200, [(b) and (f)] 80, [(c) and (g)] 40, and [(d) and (h)] 19 eV. In (e), (f), (g), and (h), interference effects are neglected, while they are included in the spectra of (a), (b), (c), and (d). All spectra are convoluted with the experimental response function.

example, for the innermost $4p$ channel (^4D) there is one such extra branch starting at $b=5.1$ and $\theta=4.1°$ for collisions at 200 eV. However, this branch and similar ones for the other $4p$ channels give rise to large scattering angles and only influence the angular distributions far out, where the single-capture cross sections are very small. The intensities in the experimental and theoretical distributions at $\theta>4°$ are very small for the 200-eV case (cf. Fig. 5). At the lower energies, the possible influence of double-capture channels lies outside the experimental acceptance. Thus for studies of the angular distributions following single-electron capture in Ar^{4+}-Ar collision below 200 eV and within our experimental acceptance, double-capture channels may be ignored.

B. True double capture

The energy-gain spectra of true double-electron capture are shown for the collision energies 300, 400, 500, and 800 eV in Fig. 11. Each spectrum contains one peak with relative energy widths ranging between 2.2% for the lowest and 1.6% for the highest energy, respectively. The centers of gravity for the energy distributions shift from 15 to 16.7 eV between the lowest and highest energy, with an estimated accuracy of ± 0.5 eV for the absolute calibration of the energy-gain scale. The kinematic energy shift is defined as the difference between the collision inelasticity Q and the projectile energy gain ΔE and is thus equal to the recoil energy of the target ion. From our simultaneously measured angular distributions we arrive at average values of $Q-\Delta E$ in accordance with the energy dependence of the double-capture energy-gain peak of Fig. 11. The present spectra indicate population of double-electron capture at $Q\sim 17$ eV for all energies, which is in agreement with the result of Koslowski and Huber[19] at 800 eV. Such a collision inelasticity indicates a total binding energy for the two electrons captured to the Ar^{4+} projectile of

$$Q+I_{Ar}+I_{Ar^+}=60.4 \text{ eV} .$$

The binding energy of ground-state Ar^{3+} with respect to Ar^{4+} is 59.8 eV and, thus, double excited Ar^{2+} states residing close to the Ar^{3+} ground state are presumably formed in 200–800-eV Ar^{4+}-Ar collisions. Koslowski and Huber[19] measured the double-capture energy-gain spectrum with a relative energy resolution of about 0.1% and deduced that many unresolved channels, within a Q range of roughly 7 eV, make up the double-capture peak at the 800-eV collision energy. The full width at half maximum intensity of their measured distribution is about 4 eV, showing the capture to Ar^{2+} states both below and above the Ar^{2+} ionization limit. Thus, the observation of double-capture energy gain centered around $Q=17$ eV indicates radiative stabilization of some of the doubly excited states formed in Ar^{4+}-Ar collisions.

In Fig. 12 the experimental angular distributions of true double-electron capture (dashed line) are compared with calculated regions of scattering angles for one- and two-step processes at the collision energies 300, 400, 500, and 800 eV. The angular distributions for single-electron capture for the same energies are shown in the same figure (solid line) at one tenth of their intensities. The interatomic potentials for two-electron processes in Ar^{4+}-Ar collisions are poorly known, in part, due to the poorly known energy term diagram of doubly excited Ar^{2+}. Thus, for two-electron angular distributions we settle for a more crude comparative calculation, using a single hypothetical double-capture channel at or close to the experimentally established maximum for the energy-gain

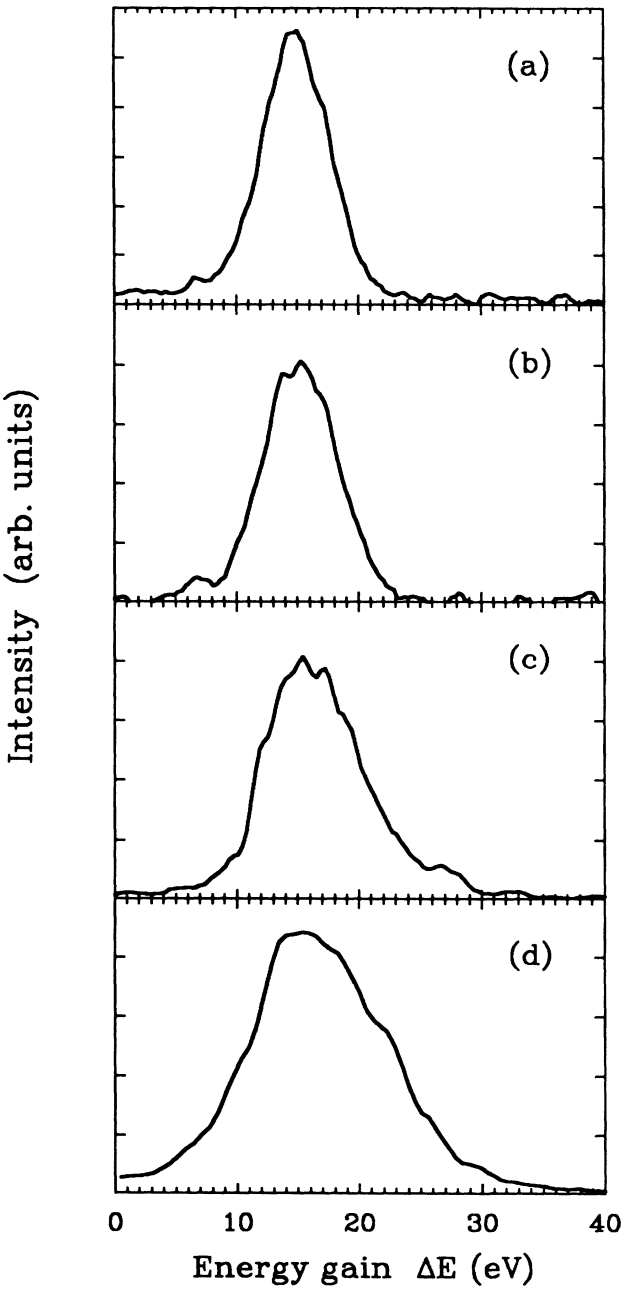

FIG. 11. Energy-gain spectra for true double capture in Ar^{4+}-Ar collisions at the energies (a) 300, (b) 400, (c) 500, and (d) 800 eV.

distributions. It is, of course, possible to calculate angular distributions with one or several assumed double-capture channels, but the value of comparisons with such calculations can be questioned since the angular distributions are quite sensitive to the actual positions (Q values) of these channels. Instead, we indicate regions of scattering angles for which a high spectral intensity can be expected for the one- and two-step processes for a double-capture channel at $Q=17$ eV or at $Q=15.5$ eV, which are both consistent with the recorded energy-gain distributions (cf. Fig. 11). The markers pointing down indicate regions for the two-step process due to a double-capture channel at $Q=15.5$ eV (upper row of Fig. 12) and $Q=17$ eV (lower row). The markers pointing up signify one-step processes (see Fig. 12). The lower limit for the one-step process populating the $Q=15.5$ eV channel is taken as the projectile scattering angle for a collision in which the radial motion is reversed at the internuclear distance of the crossing between the incident channel and the $4s\ ^2P$ channel, and with a transfer to the double-capture channel on the way out from the collision. Such a path is not possible for capture to a $Q=17$ eV channel, since it is crossing the incident channel inside the $4s\ ^2P$ one. The positions of the one-step markers (upward pointing) at the large-angle limit for the $Q=15.5$ eV channel, and the marker for the $Q=17$ eV channel, are obtained from the assumption that the turning point equals the crossing distance between the incident and the double-capture channels. The (upward pointing) marker for $Q=17$ eV, and the (upward pointing) marker at small angles for $Q=15.5$ eV, are strict lower limits for scattering in a one-step double-capture process. Clearly, the scattering angle for a one-step process might be larger than this, but the cross section is expected to decrease with increasing θ due to smaller impact parameters. The markers for the two-step double-electron-transfer processes (downward pointing) are calculated for scattering on the $4p$ single-capture potentials on the way in to the turning point and on the double-capture channel ($Q=17$ or 15.5 eV) on the way out. The markers at the large- and the small-angle limit pointing down are obtained for motion along the innermost (^4D) and outermost (^2S) of the $4p$ LS curves, respectively, where the turning points are taken as the crossings between the active $4p$ channel and the double-capture channel. The markers at small angles pointing down show strict lower limits for the two-electron processes involving the $4p$ single-capture paths.

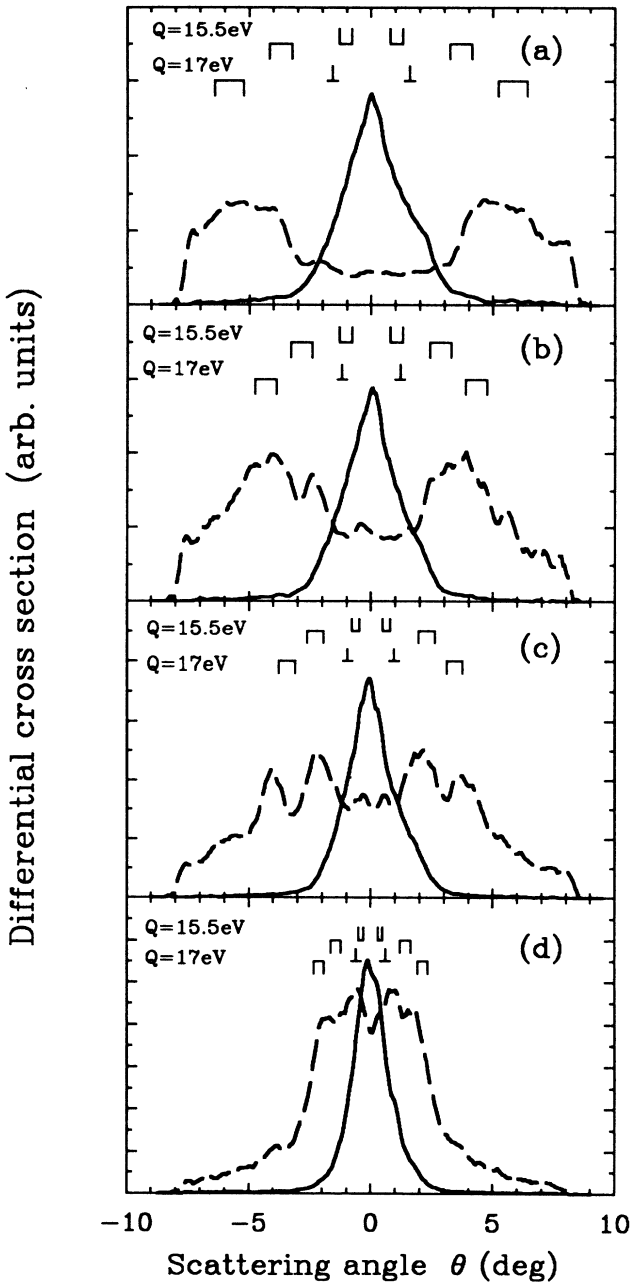

FIG. 12. Comparisons between measurements of angular distributions for double-electron capture (dashed line) and single-electron capture (solid line) in Ar^{4+}-Ar collisions at (a) 300, (b) 400, (c) 500, and (d) 800 eV. The intensities for the single-capture peaks are reduced by a factor of 10, for reasons of clarity. The calculated angular regions for double capture, extracted by means of a double-capture channel at the Q value of 17 eV, and at $Q=15.5$ eV, are indicated. The markers pointing down indicate two-step processes, while the ones pointing up give the positions for one-step processes (cf. text).

Our estimated angular ranges and lower limits for the one-step process populating hypothetical double-capture channels at 17 eV or at 15.5 eV fall within the single-capture distributions in the energy range 300–800 eV (cf. Fig. 12). There is clear evidence for the two-step mechanism for all collision energies of Fig. 12. Koslowski and Huber,[19] who measured a double-capture angular distribution in agreement with the present one at 800 eV, arrive at the same conclusion. For the slower collisions, major parts of the spectral intensities fall outside the downward pointing markers for the two-step processes at $Q=17$ eV. It is also interesting to note that the $Q=17$ eV regions pinpoint distinct features in the angular distributions for all the energies. This strongly suggests that the most intense features at, e.g., 400 eV are due to population of double-capture channels through paths on the six $4p$ single-capture potentials. At 300 eV and above, the two-step region for $Q=17$ eV falls at substantially

larger angles than the one for $Q=15.5$ eV. Thus, we do suggest that double-electron-capture channels consistent with the recorded energy-gain distributions are populated through the two-step mechanism, producing the observed large-angle maxima in the angular distributions displayed in Fig. 12. In the second step of these double-capture processes, a one-electron transition at the active $4p$ channel's crossing with the double-capture channel would populate doubly excited $4p\,(^{2S+1}L)nl\ Ar^{2+}$ terms. The principal and angular momentum quantum numbers for the capture state are denoted by n and l, respectively, and L and S specify the active $4p$ single-capture channel. For consecutive one-electron transfers the binding energies are $Q_{SC}+I_{Ar}\sim 24$ eV for the first electron ($4p$) and $Q_{DC}-Q_{SC}+I_{AR^+}\sim 36$ eV for the second one (nl), where Q_{SC} and Q_{DC} are the experimental Q values for single- and double-electron capture, respectively. Since the binding energy of the $4s\ Ar^{3+}$ state is only about 27 eV, even in the absence of an outer $4p$ electron, nl would have to be $3d$, provided that both the projectile and target cores are conserved when the second electron is transferred. A second step involving capture of one electron to the $3p$ state and a simultaneous excitation of another electron from $3s$ to $3p$ in either the projectile or the target, however, would also tie in energetically with the measured Q values. Thus, one of the two possibilities for the second step in the two-step double-capture mechanism in Ar^{4+}-Ar collisions, at which we arrive from the measurements of energy-gain and angular distributions, involves the simultaneous rearrangement of two electrons.

The double-capture angular distributions, which are cut at the edges of the detector, clearly show that the two-step process with $4p$ single-capture channels connecting the incident to the double-capture channels is dominant for the lower energies. Yet, there is a nonzero intensity at scattering angles consistent with the one-step process even at 300 eV and, as can be seen in Fig. 12, the relative intensity at forward angles increases with higher energy. It is, however, not possible to unambiguously conclude the existence of simultaneous (one-step) two-electron transfer for the present collision system. This is due to the small separation between the crossings for the double-capture channels with the incident channel and with the $4s\ ^2P$ channel. In this way, the triangle formed by the three potentials is very small (or even nonexistent) and, thereby, the difference in projectile scattering for the two paths is small. A two-step process producing scattering in this range would then proceed from the incident to the $4s\ ^2P$ channel and from this channel to the double-capture channel through the capture of another electron populating $(4s\ ^2P)nl$ doubly excited Ar^{2+} states. The following argument suggests that the two-step process is dominant also for the scattering at smaller angles: It is reasonable to assume that the crossing between the double-capture channel and the incident channel is more diabatic than adiabatic in character for collisions at 300 eV. Then the relative intensity of small-angle one-step double-capture scattering should have an energy dependence opposite to the one displayed in Fig. 12, i.e., it should decrease with increasing velocity as the reaction window moves to smaller R. When the collision energy is increased, the probability flux on the incident potential at small internuclear separations increases, as is evident from the increase of the single-capture forward rainbow scattering (cf. Fig. 5). This gives more intensity on the (adiabatic) $4s\ ^2P$ potential and thereby more intensity in the two-step forward angle double-electron-capture process, in agreement with the observed velocity dependence of forward double-capture spectral intensities in Fig. 12. Thus, assuming a one-step two-electron reaction window inside the crossings between the incident and the double-capture channels in the vicinity of 6.5 a.u. (cf. the two-electron reaction window for C^{4+}-Ne in Ref. 2), we conclude that the two-step capture mechanism dominates also for small-angle scattering.

C. Transfer ionization

The single-capture energy-gain spectra for 150- and 200-eV Ar^{4+}-Ar collisions are presented for small ($\theta<1°$) and large scattering angles ($\theta>4°$) in Fig. 13. A feature that is due to transfer ionization at an energy gain of ~ 16 eV, i.e., similar to the one for true double capture, appears at large angles. The absence of transfer ionization at small projectile scattering angles is in accordance with earlier measurements of single-capture energy-gain spectra in the forward direction.[18–20] Giese *et al.*[17] recorded a small contribution from transfer ionization at the relatively high collision energy of 2180 eV. For collision energies higher than 200 eV our experimental resolution is not sufficient to separate transfer ionization and single-electron capture. The similarity of the inelasticity distributions for transfer ionization and true double capture implies that states of similar excitations are populated. A comparison of the angular distributions due to single capture, double capture, and transfer ionization at 200 eV is shown in Fig. 14. The agreement between angular distributions for the two latter processes, which are cut off at the edges of the detector at large angles, strong-

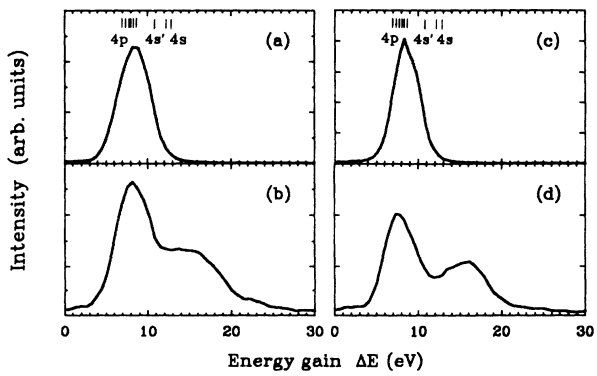

FIG. 13. Energy-gain spectra for single-electron capture in 200- and 150-eV Ar^{4+}-Ar collisions at $\theta<1°$ [(a) 200 eV, (c) 150 eV)] and at $\theta>4°$ [(b) 200 eV, (d) 150 eV]. The peaks centered at $\Delta E=16$ eV are due to transfer ionization.

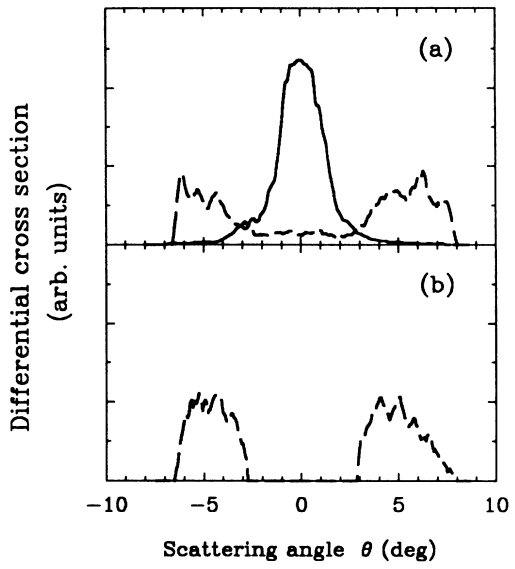

FIG. 14. Comparisons between the angular distributions of single-electron capture [(a), solid line], true double-electron capture [(a), dashed line], and transfer ionization (b) in 200-eV Ar^{4+}-Ar collisions. The single-capture peak is reduced by a factor of 10.

ly suggests that the formation of both autoionizing and nonautoionizing states are dominated by two-step electron transfer in which the $4p$ single-capture channels connect the incident and the final double-capture channels.

Insight into the mechanisms behind the rather strong dominance of true double-electron capture over transfer ionization, in spite of the experimental fact that terms that are energetically allowed to autoionize are abundantly populated, can be gained by examining the combinations of total electronic spin, parity, and angular momentum implied by the double-capture mechanisms. In Sec. IV B we argued that the present two-electron processes proceed as consecutive one-electron captures involving the $4p$ LS terms and a capture of a second electron to the $3d$ state or to the $3p$ state with a simultaneous $3s$ to $3p$ excitation. Here we restrict ourselves to the discussion of the former alternative, although similar arguments may also be applied for the latter double-capture process. For the Ar^{2+} states having excitation energies just above the Ar^{3+} ionization limit (see discussion above), the Ar^{3+} continua are all based on the $^4S^o$ Ar^{3+} ground state and the eigenvalues of the total angular momentum L and parity π operators are both determined by the angular momentum l' of the continuum electron. Continua, which are energetically available for electron emission of such Ar^{2+} states, are thus triplets or quintets with $L=l'$ and $\pi=(-1)^{(l'+1)}$ (i.e., S^o,P^e,D^o,F^e,G^o). Capture to the $3d$ state of Ar^{3+} in any of the six $4p$ ^{2S+1}L terms, all of odd parity, would populate odd Ar^{2+} states. This means that the odd P and F Ar^{2+} terms that are formed in $3d$ capture to the $4p$ $^{2,4}P$ and $4p$ $^{2,4}D$ single-capture states cannot decay through autoionization (even if they are excited above the Ar^{3+} ionization limit) due to the parity and angular momentum conservation rules. Moreover, capture to the doublet $4p$ LS terms may form triplet and single states, of which the latter are forbidden to autoionize due to the spin-selection rule for Coulomb autoionization. This readily explains why a majority of the Ar^{2+} states, formed in the two-step two-electron transfer processes, charge-state stabilize (through photon emission), even though the measured distributions of Q values indicate that a fair fraction is excited above the Ar^{3+} ionization limit. At 200 eV and within the present angular acceptance, we find that true double-electron capture dominates over transfer ionization by roughly one order of magnitude.

V. SUMMARY AND CONCLUSION

In this work we present data for single-electron capture, true double-electron capture, and transfer ionization in the energy range 19–800 eV. We provide an Ar^{4+} beam of narrow energy distribution and small angular divergence at intensities ranging between 10^3 and 10^4 particles per second for the lower and upper parts of the collision-energy regime, respectively. From the energy-gain measurements we conclude that only $4p$ states are populated in single-electron capture at the lower end of the velocity range and we find strong experimental evidence that the $4s'$ (^1D $4s$ ^2D) channel is passed diabatically over the whole velocity range and that the $4s$ ^2P channel acts as an inner repulsive wall. The oscillatory structures seen in the experimental angular distributions are reproduced by the calculations for all energies investigated and are due to multiple rainbow scattering associated with reflection from the $4s$ ^2P state for the forward rainbow and from the five inner of the six $4p$ LS terms for the secondary intensity maximum. Calculations for different assumptions concerning the Ar^{4+}-Ar interatomic potentials show that the forward rainbow peak is very sensitive to the shape of the potential of the incident channel, while the secondary peak is not. The agreement between the present experimental and theoretical angular distributions lends credibility to our proposed reduction of semiempirical off-diagonal diabatic matrix elements.

We have shown that the dominant true double-capture electron-transfer process is a two-step mechanism proceeding along the $4p$ single-capture channels, which in turn couple to double-capture channels in the vicinity of $Q=17$ eV. We suggest that the structures in the double-capture angular distributions are due to several unresolved channels, which are the different terms formed when adding a $3d$ electron to the six $4p$ ^{2S+1}L single-electron-capture terms. However, we also point out that the energy-gain spectra do not rule out the possibility that the second step in the present two-step double-capture process is simultaneous capture (to $3p$) and excitation (from $3s$ to $3p$). This matter might be resolved through calculations of excitation energies for $(3p^3)3d4p$ and $(3s3p^4)3p4p$ Ar^{2+} configurations. It is not possible to determine whether the double-capture intensity measured at forward angles is due to a one-step process or a two-step process mediated through the outer of the $4s$ states. An argument based on the collision-energy dependence for forward-scattered double capture suggests the

two-step process. The dominance of double capture over transfer ionization at the measured Q values below 17 eV is explained as due to radiative stabilization of doubly excited Ar^{2+} states which are prohibited to decay through Coulomb autoionization by the angular momentum, spin, and parity selection rules. The similarity of angular distributions for double-electron capture and transfer ionization shows that doubly excited states populated through the six $4p$ LS single-capture channels are formed through the same electron-transfer mechanism in both processes.

We have presented further support for the domination of consecutive one-electron transfers in multiple-electron-capture mechanisms, which is one of the fundamental assumptions of, e.g., the extended classical over-barrier model.[22] The present work also underscores the need for further coordinate development of experiments and theory to elucidate charge-transfer mechanisms in slow and, especially, very-slow collisions between highly charged ions and atoms. It is evident that more work is needed on simple collision systems having well-known energy-level diagrams and few active channels. Knowledge of excitation energies, decay rates, and branching ratios in doubly excited systems of high charge is far from complete, although access to such parameters is essential for the understanding of fundamental collision dynamics. Experimental and theoretical data on highly charged ions with two or more electrons in excited states are thus very much needed.

ACKNOWLEDGMENTS

The work was supported in part by the National Science Foundation; by the U.S. Department of Energy, Office of Basic Energy Sciences, Division of Chemical Sciences, under Contract No. DE-AC05-84OR21400 with Martin Marietta Energy Systems Inc; and by the Swedish Natural Science Research Council.

[1]H. Cederquist, G. Astner, A. Bárány, H. Danared, A. Johnson, L. Liljeby, K.-G. Rensfelt, S. Huldt, P. Hvelplund, and H. Knudson, Nucl. Instrum. Methods B **24/25**, 43 (1987).

[2]H. Cederquist, L. H. Andersen, A. Bárány, P. Hvelplund, H. Knudsen, E. H. Nielsen, J.O. K. Pedersen, and J. Sorensen, J. Phys. B **18**, 3951 (1985).

[3]P. Benoit-Cattin, A. Bordenave-Montesquieu, M. Boudjema, A. Gleizes, S. Dousson, and D. Hitz, J. Phys. B **21**, 3387 (1988).

[4]T. Bouchama, M. Druetta, and S. Martin, J. Phys. B **22**, 71 (1989).

[5]P. Roncin, M. Barat, M. N. Gaboriaud, L. Guillemot, and H. Laurent, J. Phys. B **22**, 509 (1989).

[6]E. Y. Kamber, C. L. Cocke, J. P. Giese, J. O. K. Pedersen, and W. Waggoner, Phys. Rev. A **36**, 5575 (1987).

[7]J. Tan, C. D. Lin, and M. Kimura, J. Phys. B **20**, L91 (1987).

[8]H. Cederquist, C. Biedermann, J. C. Levin, C.-S. O, I. A. Sellin, and R. T. Short, Nucl. Instrum. Methods B **34**, 243 (1988).

[9]H. Cederquist, L. Liljeby, C. Biedermann, J. C. Levin, C.S. O, H. Rothard, K.-O. Groeneveld, C. R. Vane, and I. A. Sellin, Phys. Rev. A **39**, 4308 (1989).

[10]C. Biedermann, H. Cederquist, J. C. Levin, R. T. Short, L. Liljeby, L. R. Andersson, H. Rothard, K.-O. Groeneveld, C.-S. O, C. R. Vane, J. P. Gibbons, S. B. Elston, and I. A. Sellin, in *Invited talk at the Sixteenth International Conference on the Physics of Electronic and Atomic Collisions, New York, 1989*, edited by A. Dalgarno, R. S. Freund, M. S. Lubell, and T. B. Lucatorto (AIP, New York, in press).

[11]D. A. Church and H. M. Holzscheiter, Phys. Rev. Lett. **49**, 643 (1982).

[12]C. C. Havener, M. S. Huq, H. F. Krause, P. A. Schultz, and R. A. Phaneuf, Phys. Rev. A **39**, 1725 (1989).

[13]H. Laurent, M. Barat, M. N. Gaboriaud, L. Guillemot, and P. Roncin, J. Phys. B **20**, 6581 (1987).

[14]P. Roncin, M. N. Gaboriaud, M. Barat, and H. Laurent, Europhys. Lett. **3**, 53 (1987).

[15]L. N. Tunnell, C. L. Cocke, J. P. Giese, E. Y. Kamber, S. L. Varghese, and W. Waggoner, Phys. Rev. A **35**, 3299 (1987).

[16]W. Waggoner, C. L. Cocke, L. N. Tunnell, C. C. Havener, F. W. Meyer, and R. A. Phaneuf, Phys. Rev. A **37**, 2386 (1988).

[17]J. P. Giese, C. L. Cocke, W. Waggoner, L. N. Tunnell, and S. L. Varghese, Phys. Rev. A **34**, 3770 (1986).

[18]J. Puerta, H.-J. Kahlert, H. R. Koslowski, and B. A. Huber, Nucl. Instrum. Methods B **9**, 415 (1985).

[19]H. R. Koslowski and B. A. Huber, J. Phys. B **22**, 2255 (1989).

[20]P. Hvelplund and H. Cederquist (unpublished).

[21]H. Ryufuku, K. Sasaki, and T. Watanabe, Phys. Rev. A **21**, 745 (1980).

[22]A. Bárány, G. Astner, H. Cederquist, H. Danared, S. Huldt, P. Hvelplund, A. Johnson, H. Knudsen, L. Liljeby, and K. G. Rensfelt, Nucl. Instrum. Methods B **9**, 397 (1985).

[23]P. Hvelplund, L. H. Andersen, A. Bárány, H. Cederquist, J. Heinemeier, H. Knudsen, K. B. MacAdam, E. H. Nielsen,and J. Sorensen, Nucl. Instrum. Methods B **9**, 421 (1985).

[24]P. Hvelplund, A. Bárány, H. Cederquist, and J. O. K. Pedersen, J. Phys. B **20**, 2515 (1987).

[25]R. K. Janev and H. Winter, Phys. Rep. **117**, 265 (1985).

[26]R. E. Olson and A. Salop, Phys. Rev. A **14**, 579 (1976).

[27]K. Taulbjerg, J. Phys. B **19**, L367 (1986).

[28]A. Bordenave-Montesquieu, P. Benoit-Cattin, A. Gleizes, A. I. Marrakchi, S. Dousson, and D. Hitz, J. Phys. B **17**, L223 (1984).

[29]N. Stolterfoht, C. C. Havener, R. A. Phaneuf, J. K. Swenson, S. M. Shafroth, and F. W. Meyer, Phys. Rev. Lett. **57**, 74 (1986).

[30]H. Winter, M. Mack, R. Hoeckstra, A. Niehaus, and F. J. de Heer, Phys. Rev. Lett. **58**, 957 (1987).

[31]N. Stolterfoht, C. C. Havener, R. A. Phaneuf, J. K. Swenson, S. M. Shafroth, and F. W. Meyer, Phys. Rev. Lett. **58**, 958 (1987).

[32]J. C. Levin, R. T. Short, C.-S. O, H. Cederquist, S. B. Elston, J. P. Gibbons, and I. A. Sellin, Phys. Rev. A **36**, 1649 (1987).

[33]R. Hippler, K. Saeed, A. J. Duncan, and H. Kleinpoppen, Phys. Rev. A **30**, 3328 (1984).

[34]C. L. Cocke, Phys. Rev. A **20**, 749 (1979).

[35]J. B. Marion and F. C. Young, *Nuclear Reaction Analysis Graphs and Tables* (Elsevier, New York, 1968), p. 142.

[36]L. R. Andersson, J. O. P. Pedersen, A. Bárány, J. P. Bangsgaard, and P. Hvelplund, J. Phys. B **22**, 1603 (1989).

[37]R. E. Johnson, *Introduction to Atomic and Molecular Collisions* (Plenum, New York, 1982).

[38]M. S. Child, in *Atomic and Molecular Collision Theory,* edited by F. A. Gianturco (Plenum, New York, 1982).
[39]H. R. Koslowski, B. A. Huber, and V. Staemmler, J. Phys. B **21**, 2923 (1988).
[40]M. Kimura, T. Iwai, Y. Kaneko, N. Kobayashi, A. Matsumoto, S. Ohtani, K. Okuno, S. Tagaki, H. Tawara, and S. Tsurubuchi, J. Phys. Soc. Jpn. **53**, 2224 (1984).
[41]R. Grice and D. R. Herschbach, Mol. Phys. **27**, 159 (1974).
[42]M. Gargaud and R. McCarroll, J. Phys. (Paris) Colloq. **50**, C1-127 (1989).
[43]P. Roncin, M. N. Gaboriaud, H. Laurent, and M. Barat, J. Phys. B **19**, L691 (1986).